# Cation binding to SERCA

B Sun, BD Stewart,AN Kucharski, PM Kekenes-Huskey*

December 29, 2018

**Abstract**

Sarcoendoplasmic reticulum $Ca^{2+}$-ATPase (SERCA) is a transmembrane pump that plays an important role in transporting calcium into the sarcoplasmic reticulum (SR). While calcium ($Ca^{2+}$) binds SERCA with micromolar affinity, magnesium ($Mg^{2+}$) and potassium ($K^+$) also compete with calcium ($Ca^{2+}$) binding. However, the molecular bases for these competing ions' influence on SERCA function and the selectivity of the pump for $Ca^{2+}$ are not well-established. We therefore used *in silico* methods to resolve molecular determinants of cation binding in the canonical site I and II $Ca^{2+}$ binding sites: 1) triplicate molecular dynamics (MD) simulations of $Mg^{2+}$, $Ca^{2+}$and $K^+$-bound SERCA. 2) mean spherical approximation (MSA) theory to determine the affinity and selectivity of cation binding to the MD-resolved structures and 3) state models of SERCA turnover informed from MSA-derived affinity data. Our key findings are that a) coordination at sites I and II are optimized for $Ca^{2+}$and to a lesser extent for $Mg^{2+}$ and $K^+$, as determined by MD-derived cation-amino acid oxygen and bound water configurations, b) the impaired coordination and high desolvation cost for $Mg^{2+}$ precludes favorable $Mg^{2+}$ binding relative to $Ca^{2+}$, while $K^+$ has limited capacity to bind site I, c) $Mg^{2+}$ most likely acts as inhibitor and $K^+$ as intermediate in SERCA's reaction cycle, based on a best-fit state model of SERCA turnover. These findings provide a quantitative basis for SERCA function that leverages molecular-scale thermodynamic data and rationalize enzyme activity across broad ranges of $K^+$, $Ca^{2+}$ and $Mg^{2+}$ concentrations.

# 1 Introduction

sarcoendoplasmic reticulum $Ca^{2+}$-ATPase (SERCA) is a 110-kDa transmembrane cation pump which actively transports $Ca^{2+}$ ions into the SR by utilizing energy released from adenosine triphosphate (ATP) hydrolysis [1]. SERCA has been widely studied for its role in returning intracellular $Ca^{2+}$ to basal levels following stimuli that elevate$Ca^{2+}$ content [2]. The pump's catalytic cycle is roughly characterized by four states comprising a sequential cycle $E1 \rightarrow E1P.2Ca \rightarrow E2P.2Ca \rightarrow E2$. In E1, the $Ca^{2+}$ binding sites are exposed to the cytosolic space, whereas the E2 conformations expose the low-affinity $Ca^{2+}$ sites toward the SR lumen. The transition between E1 and E2 is driven by ATP hydrolysis at residue Asp 351 [1] following $Ca^{2+}$ binding, for which E1P and E2P are the respective phosphorylated states of the enzyme. Accompanying transitions between catalytic states are prominent changes in its ten transmembrane (TM) helices as well as the cytosolic actuator (A) domain, nucleotide-binding domain (N) and phosphorylation domain (P). Many of these changes have been resolved through x-ray crystallography [3–6].

Based on available structural models of the protein and a wealth of biochemical studies [7–14], reactions schemes linking the E1 and E2 states are beginning to emerge. Utilizing SERCA vesicles coupled with spin label molecule, Inesi et al observed changed electron spin resonance spectrum upon $Ca^{2+}$ binding that revealed conformational changes in the enzyme [11]. Dupont and coworkers similarly measured changes in intrinsic fluorescence upon $Ca^{2+}$ bind-

ing and further proposed a two-step $Ca^{2+}$ binding process to high affinity sites evidenced by the pumps slow rate of fluorescence changes [9, 10]. Additionally, conformational changes linking the E1 and E2 states were explored by kinetic studies of intrinsic fluorescence changes upon $Ca^{2+}$ binding and release [7, 8]. To probe molecular determinants of $Ca^{2+}$ binding in the pump, an E309Q mutant bound with two $Ca^{2+}$ in its phosphorulated state was determined via x-ray crystallography [15], which revealed the altered TM arrangements caused by the mutation leads to impaired pump functionality. With respect to cation binding affinities, Inesi et al measured $Ca^{2+}$ binding and stoichiometry to SERCA vesicles in via chromatography [16], while others have probed the binding of the non cognate $Mg^{2+}$ and $K^{+}$ ions via intrinsic fluorescence changes in SERCA [17, 18].

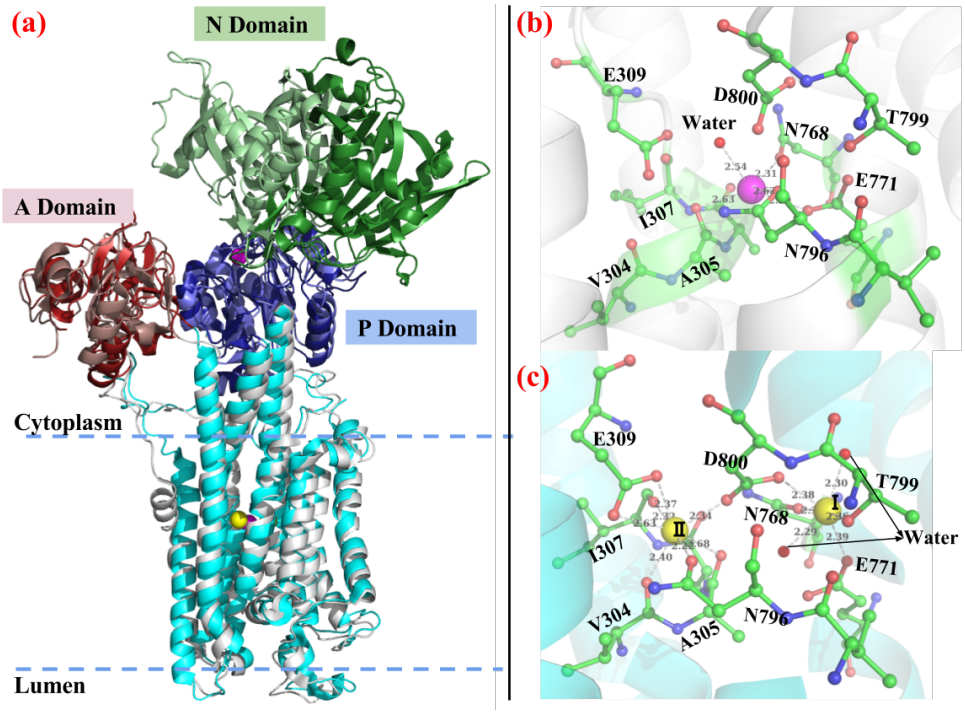


Figure 1: [figshort:crystalstr]Comparison of $Ca^{2+}$-bound (PDB ID: 1su4) and $Mg^{2+}$-bound (PDB ID: 3w5b) SERCA crystal structures. (a) Superimpose of two crystal structures with 1su4/3w5b cytosolic domains (A, P and N) colored in red/salmon, blue/slate and green/palegreen. The TM helices are colored in cyan and grey for 1su4 and 3w5b, respectively. (b-c) $Mg^{2+}$ and $Ca^{2+}$ binding site comparison. In this orientation, sites I and II are right and left, respectively. $Mg^{2+}$ and $Ca^{2+}$ are represented as magenta and yellow balls. The distance between coordination oxygen atom and cation are also shown. The oxygen atoms of crystal water molecules are shown as red balls.

In complement to experiment, extensive molecular dynamics simulations have uncovered many aspects of cation binding and SERCA function that are difficult to probe via experimental approaches. Huang et al first explored the $Ca^{2+}$ binding pathways to SERCA TM sites via MD simulation and observed the cooperative binding of two $Ca^{2+}$ ions [19]. Kekenes-Huskey et al performed MD simulations on SERCA with and in the absence of $Ca^{2+}$ to examine gating of $Ca^{2+}$ binding by E309 [20], in addition to estimating ion binding free energies and kinetics. Espinoza-Fonseca et al evaluated the interaction energy between $Ca^{2+}/Mg^{2+}/K^{+}$ and SERCA binding sites based on MD trajectories and reported that $Ca^{2+}$ has the most negative interaction energy while $K^{+}$ has the least negative value [21]. Besides these computational work focusing on cation binding, other more recent studies have probed mechanism of normal SERCA function and it's modulation by regulatory proteins [22–26].

Although studies have been reported on the roles of $Mg^{2+}$, $K^{+}$ on SERCA binding, less has been done to provide a thermodynamic basis for their effects on SERCA function. This is of particular importance, as intracellular $K^{+}$ and $Mg^{2+}$ concentrations are orders of magnitude larger than the roughly sub micromolar $Ca^{2+}$ concentrations found in typical cells. Here, simulation studies of cation binding to molecular sites that resemble high affinity, amino acid-based motifs have been informative. Dudev et al for instance constructed cation binding sites using model compounds and calculated cation binding energies via quantum mechanics [27]. Ye et al designed a theoretical framework in combination with MD simulations to calculate cation binding free energies and isolate the energetic contribution from geometric and confinement effect [28]. Implicit models that describe $Ca^{2+}$ binding thermodynamics as via ion density-based formalisms have also been reported, including reference interaction site modeling [29] and density functional theory [30]. Besides these methods relied on explicit binding site configurations, Nonner et al developed the MSA model in which the binding site is treated as confined filter filled with coordination oxygens. A variant of density functional theory called the mean spherical approximation (MSA) approach has proven effective in rank-ordering the binding of cationic species to oxygen-rich binding domains such as EF-hands in $\beta$ parvalbumin ($\beta$-PV) [31] and $Ca^{2+}$ channel selectivity filters [32, 33], through describing the electrostatics and hard-sphere contributions to the chemical potential of partitioning ions into oxygen-rich 'filters'.

Our study has therefore focused on the 1) the selectivity of $Ca^{2+}$ versus $Mg^{2+}$ and $K^{+}$ and 2) the combination of molecular dynamics (MD) derived date with thermodynamic state-based models to assess contributions of $Mg^{2+}$ and $K^{+}$ binding on the SERCA turnover rate. Here we performed MD simulations of $Ca^{2+}$, $Mg^{2+}$ and $K^{+}$-bound wild-type (WT) SERCA as well as the E309Q and N796A variants. These MD data provided structural information to assess cation binding thermodynamics via MSA to elucidate the molecular basis of SERCA's preference of $Ca^{2+}$ over $Mg^{2+}$ and $K^{+}$. Further, we relate these studies of E1 state ion binding to a state-based kinetic model of SERCA pump rate to determine the extents to which $Mg^{2+}$ and $K^{+}$ facilitate or inhibit catalysis. With this approach, we provide a multiscale and molecular basis for cation binding to SERCA and impacts on pump function.

# 2 RESULTS

## 2.1 Molecular dynamics simulations

We performed triplicate simulations of wild-type SERCA and its variants E309Q and N768A to probe the binding site coordination of the cations $Ca^{2+}$, $Mg^{2+}$ and $K^{+}$. $Ca^{2+}$- and $Mg^{2+}$-bound configurations of the proteins have been determined through x-ray crystallography, but to our knowledge, the binding of $K^{+}$ to the $Ca^{2+}$ binding domain has only been resolved via simulation [21]. In Fig. S1 we verify that the root mean squared deviations (RMSD)s of the peptide backbone atoms comprising the TM helices are relatively small (with $Ca^{2+}$-bound cases around 1.1 Å and $Mg^{2+}/K^{+}$-bound cases around 1.5 Å) and do not significantly deviate from the input x-ray structures, suggesting that structures are near a local minimum. As shown in Fig. S2, the TM helices are quite similar across the cases considered, with minor deviations localized to the $Ca^{2+}$-binding region. We note that the cytosolic A, N and P domains exhibit greater RMSD values (Fig. S3), which agrees with previous analyses of the $Ca^{2+}$ bound system [20, 21]. Although these domains were dynamic, they largely preserved the approximately 50 Å and 40 Å A-N domain distances in the input structures, as measured between the center of mass (COM) of A domain (residues 1-47/123-240) and N domain (residues 358-603). Overall, the predicted $Ca^{2+}$-bound variants and $Mg^{2+}$-bound systems are consistent with previous structural [3, 34] and simulation [20, 21] studies.

We additionally report the root mean squared fluctuations (RMSF) of TM and cytosolic domain residues in Fig. 2 and Fig. 3, respectively as a qualitative gauge of the proteins' stability.

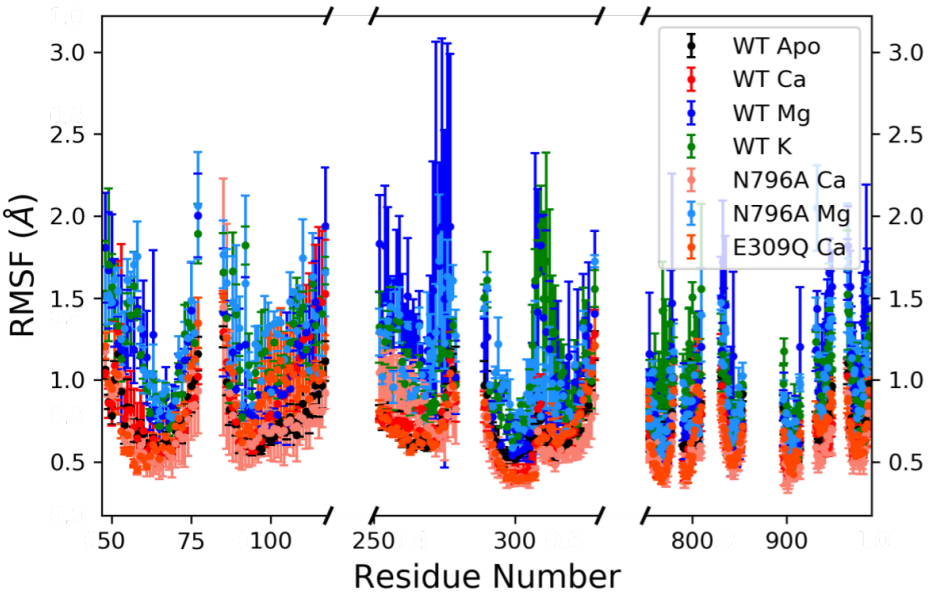


Figure 2: [figshort:tmrmsf]Heavy atom RMSF of each residue in the ten TM helices during the simulation. The trajectories were first aligned based on the TM backbone before RMSF calculations. The error bars are calculated from the triplicate trajectories for each case. The gaps represent cytosolic domains which are plotted in Fig. 3.

As shown in Fig. 2, the overall RMSF of all TM domains are small, with values of up to 3 Å attributed to TM3 in the WT $Mg^{2+}$-bound case. In contrast, the $Ca^{2+}$-bound cases yield the smallest RMSF values (approximately 1 Å), indicating that the TM regions are quite immobile when stabilized by bound $Ca^{2+}$. However, the cytosolic domains yield larger RMSF values as shown in Fig. 3, most notably for the A and N domains (5 Å), which demonstrates significant mobility of cytosolic domains versus theTM region in agreement with previous studies [20, 21]. As shown in previous studies, the domain motions are well-characterized as an opening/closing that we report as an A-N interdomain distance (Fig. 3(d)). Our simulations generally reflected A-N distances that were close to the input structures in contrast to previous studies, which we attribute to the comparatively smaller simulation windows used in this study (100 ns versus $>$ 500 ns) For the $K^{+}$-bound case, the simulations yield similar A-N distances as the $Mg^{2+}$-bound cases, given that the $Mg^{2+}$-bound x-ray structure PDB 3w5b served as the input structure for this configuration [21]. Overall, these RMSD and RMSF data are consistent with prior MD studies of WT SERCA [20, 21].

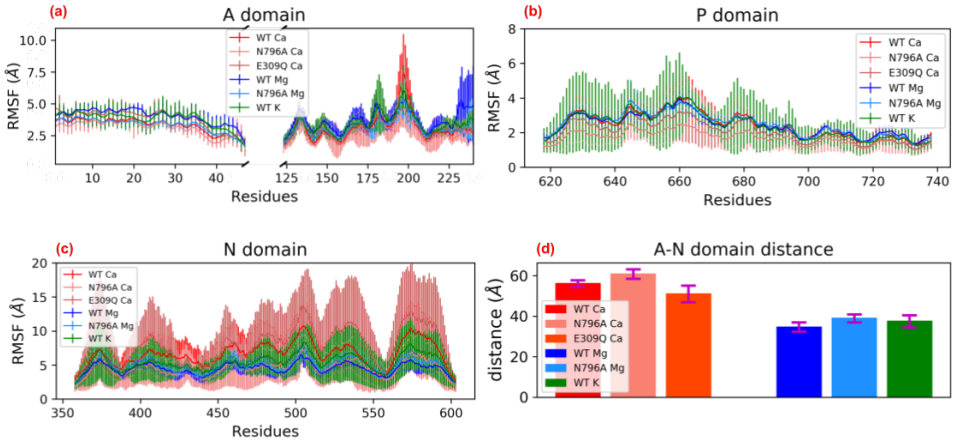


Figure 3: [figshort:cytormsf](a-c) Heavy atom RMSF of each residue in the cytosolic domain for WT and mutant SERCA during the simulation. The trajectories were first aligned based on the TM backbone before RMSF calculations. The error bars are calculated from the triplicate trajectories for each case. (d) Distance between the COMs of A and N domains.

## 2.2 Cation coordination in the $Ca^{2+}$ binding region

In this study, we highlight structural and dynamic contributions of the $Ca^{2+}$, $Mg^{2+}$ binding domains to the thermodynamics of ion binding. This is analogous to our approach for probing $Ca^{2+}/Mg^{2+}$-binding to the $\beta$ parvalbumin ($\beta$-PV) protein [31], for which we used MDsimulation-derived structural data from the cation-bound configurations to parameterize the MSA model. Specifically, we used the radius of the ions' inner coordination sphere and amino acid oxygens comprising the sphere to estimate the binding site volume and coordinating oxygen density for MSA. We use a similar strategy for SERCA in that we assess the coordination of a given ion based on the number of oxygens within six Å of the bound ion. In contrast to our previous study, we additionally include coordinated waters in the MSA calculation.

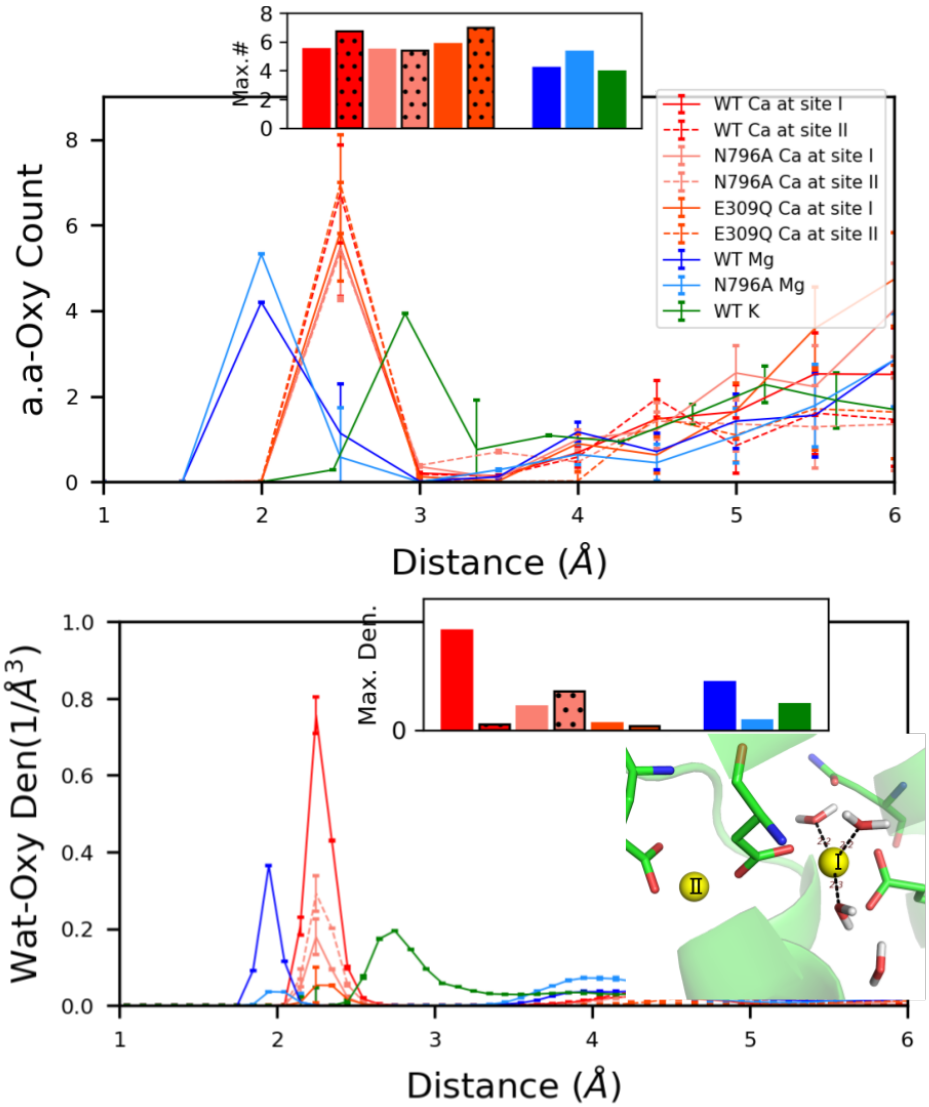


Figure 4: [figshort:aawat] radial distribution function of amino acid oxygen atoms and water oxygen atom around $Ca^{2+}/Mg^{2+}/K^{+}$. The distribution around $Ca^{2+}$ for each individual case are shown in Fig. S9 for clarity. The insets bar graph show the maximum number of coordinating amino acid oxygen and water density around cation in each case (the bars with black dots represent site II $Ca^{2+}$). The coordinating waters with site I $Ca^{2+}$ of WT SERCA is also shown.

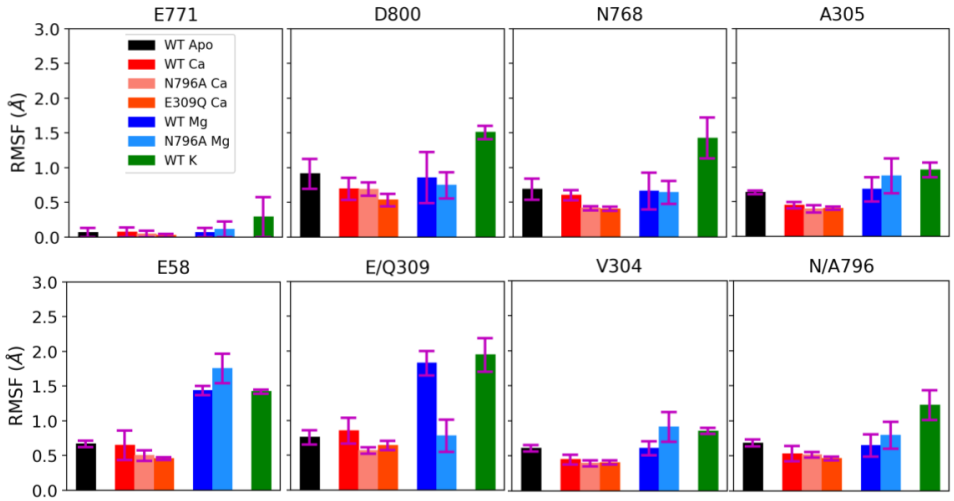


Figure 5: [figshort:keyrmsf]Heavy atom RMSF of key coordinating residues at the cation binding sites. The error bars were calculated from the triplicate trajectories for each case. The upper row represents site I residues while lower row were site II residues (E58 was not involved into coordination with cations in crystal structure, however, in the variants, it coordinated with $Ca^{2+}$ in site II, see Fig. S11).

In Fig. 4 we report radial distribution function (RDF)s of cation-coordinating oxygens during the simulation. Our simulations demonstrate that $Ca^{2+}$, $Mg^{2+}$, and $K^{+}$ have varying degrees of coordination with amino acid oxygens within the binding site. We summarize the identity of the coordinating amino acids in Sect. S1.5, although from the perspective of MSA theory, only the number of contributed amino acid oxygens is important. The $Ca^{2+}$ within site I was optimally coordinated with 8.5 oxygens on average (including three water oxygens). $Ca^{2+}$ within site II had no coordinated water oxygens but maintain six amino acid oxygens as the x-ray crystal structure. By virtue of having more coordinating oxygens, we speculate that the $Ca^{2+}$ ion in site I is bound more tightly than that found within site II. For the N796A mutant, the $Ca^{2+}$ within site I had six oxygens optimally coordinated on average which is less than that in WT site I. Interestingly, in site II, the mutation of N796 to A796 disrupted the side chain coordination with $Ca^{2+}$, however, E58 and a water molecule participated to coordinate with $Ca^{2+}$, resulting seven oxygens (see Fig. S11(b)) which is more than the six oxygens in WT type. For $Ca^{2+}$ binding this demonstrates that the N796 residue plays a part into the binding of ions within the SERCA protein, but more importantly, N796A mutant may have a lower $Ca^{2+}$ affinity at site I since less oxygens coordinates with site I $Ca^{2+}$ in N796A mutant. For the E309Q mutant, two different possible side chain rotamers of Q309 were investigated, as both rotamers were viable starting positions (see Fig. S11(c-d) for illustration of rotatmer directions). After running the simulation, the two rotamers had identical $Ca^{2+}$ coordination patterns for the two binding sites: site I had six coordinating oxygens while site II had seven and both sites had no coordinated water molecules (see Fig. S11(c-d)). Additionally, similar to the N796A site II $Ca^{2+}$ cases, E58 in TM1 also participated into the coordination with $Ca^{2+}$ at site II in both rotamers of E309Q.

$Mg^{2+}$ binds in a 'hybrid' site between sites I and II with average six coordinating oxygens (including one water molecule, see Fig. S13(a)). $K^{+}$ in site I has stable binding with five coordinating oxygens (including one water molecule, see Fig. S13(c)) while $K^{+}$ at site II is highly dynamic.

The differences of cation-oxygen coordination patterns across all cases are also reflected in mobility of coordinating residues as shown in Fig. 5. The upper row represents site I residues while lower row were site II residues. Generally, $Ca^{2+}$-bound systems have RMSF values for most residues around 0.5 Å, which are lowest among all cases. Interestingly, we did not observed RMSF decrease for apo vs. $Ca^{2+}$-bound cases. One possible reason is that in apo state significant amount of waters fill in the binding sites and stabilize residues via hydrogen bonding network (see Fig. S7). Additionally, the WT and variants shown negligible difference in RMSF upon $Ca^{2+}$ binding. However, binding of non-cognate $Mg^{2+}$ and $K^{+}$ leads to RMSF increase for all residues, with $K^{+}$ case being more obvious as most residues have RMSF larger than 1 Å. The relatively larger RMSF for $Mg^{2+}$ and $K^{+}$-bound may suggest that ion is not well-coordinated. We furthermore note that the coordination is dynamic, with distances that vary on a nanosecond timescale (see Fig. S6).

## 2.3 Thermodynamics of ion binding at sites I and II

Molecular dynamics simulations provide qualitative insight to the binding of various ions in the binding sites of SERCA, but alone do not directly predict affinities. Therefore we explored MSA to quantitatively estimate free energies and selectivity of various ion binding. MSA predicts chemical potentials of partitioning into binding site, assuming a similar approach that was performed for the $\beta$-PV [31] protein, the chemical potential of the various ions in the binding site were probed, e.g., based on a statistical mechanical description of concentrated electrolyte solutions, finite sized ions and electrostatic interactions.

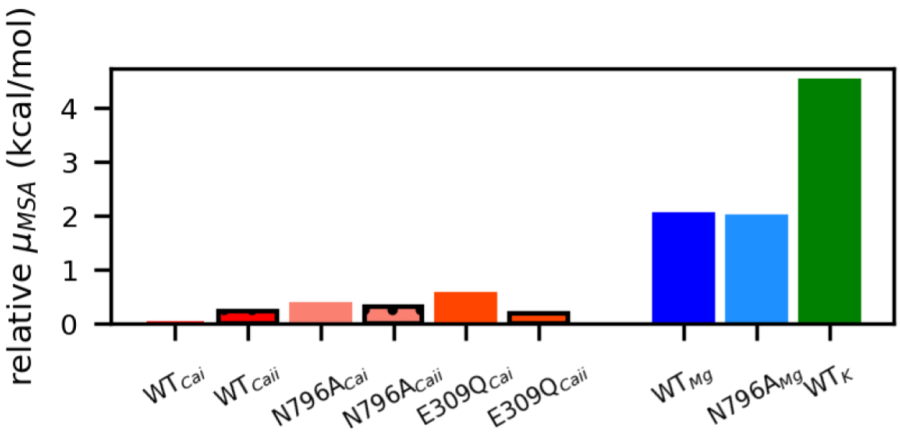


Figure 6: [figshort:msamu]MSA predicted chemical potential for each cation based on oxygen-coordination pattern (waters included) and optimal filter volumes derived from MD simulations. The shown values are relative potentials with respect to WT $Ca^{2+}$ at site I.

In this section we utilize the amino acid and water oxygen RDFs to estimate the oxygen filter densities and volumes, from which chemical potentials of ion partition into filter from solvent is estimated via MSA. As shown in Fig. 6, $Ca^{2+}$ at site I of WT case has lowest MSA predicted chemical potentials across all cases, corresponding to the largest number of coordination oxygens. For variants, site I and site II $Ca^{2+}$ ions have less favourable chemical potentials compared with site I $Ca^{2+}$ from WT cases, as the relative values are around 0.3 kcal/mol. These are consistent with the comparable $Ca^{2+}$ coordination numbers present among variants. Compared with $Ca^{2+}$-binding, $Mg^{2+}$ binding at WT and mutant SERCA has obviously unfavourable potentials as relative values being 2 kcal/mol. Among all cases, $K^+$ relative potential is most positive at 4.2 kcal/mol, indicating that $K^+$ is most thermodynamically unfavourble at TM sites. For $Mg^{2+}$ and $K^+$, the MSA predicted potentials also correlates with the cation-coordination patterns as these two ions have obviously reduced coordination number when compared with $Ca^{2+}$. Site I confers greater $Ca^{2+}$ affinity due to extensive inclusion of water coordination, trends can be rationalized using MSA theory.

In order to achieve more thorough understanding regarding energetic contribution from water, we analyzed thermodynamic properties of coordinating water sites during MD via Grid Inhomogeneous Solvation Method (GIST) model. As shown in Fig. 7, around site I $Ca^{2+}$, WT has three groups of water sites with $-12$ kcal/mol stability while N796A has one and E309Q has almost zero. These three groups of water sites in WT satisfy coordination distance with $Ca^{2+}$ and correspond to the three coordinating water molecules as shown in Fig. 4, implying that these water coordinations considerably enhance $Ca^{2+}$ affinity at site I in WT case. We also reported the GIST results for site II $Ca^{2+}$ as shown in Fig. S8. In WT and E309Q cases, these is no stable water sites within appropriate distance to $Ca^{2+}$, however, for N796A, one group of water sites with $-12$ kcal/mol stability presents and stabilizes $Ca^{2+}$ at around 3.3 Å. Since the numbers of amino acid oxygens for WT/E309Q are comparable and greater than N796A, the additional stable water site group in N796A could make the site II $Ca^{2+}$ binding affinity comparable among WT and variants. Therefore, it is evident that both coordinated amino acid oxygens and bound waters contribute to cation affinities in WT and mutant SERCA. Further, coordinated waters may compensate for the inability to optimally bind cations in sites I and II, owing to structural limitations.

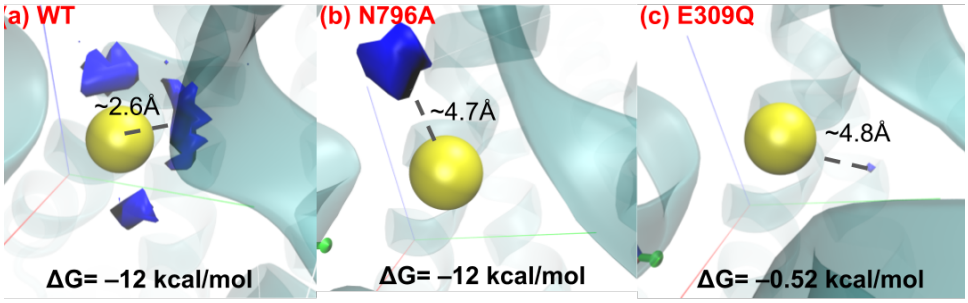


Figure 7: [figshort:site1cagist]Free energy of water sites around site I $Ca^{2+}$ calculated by GIST. For WT and N796A, the blue isosurface corresponds to water sites with $\Delta G = -12$ kcal/mol, while for E309Q the middle value of $\Delta G$ (range is $-1.03$ to 0 kcal/mol) is shown. The distance between $Ca^{2+}$ and isosurface is also shown. The site II $Ca^{2+}$ data is in Fig. S8.

The membrane into which SERCA is embedded is negatively charged [35]. The presence of membrane electrical potential would change ion concentration around SERCA, thus in principal affect the cation binding affinity. In principle, higher ionic strength should reduce desolvation terms, but it will also attenuate the bound-state electrostatic interactions. According to the Debye layer theory, the effective ion concentration near the membrane is $[i]_{eff} = e^{-\beta Z_i \zeta}[i]_{bath}$ where $Z_i$ is the charge of ion and $\beta = \frac{1}{k_b T}$, $[i]_{bath}$ is ion concentration in bath and $\zeta$ is membrane potential. Assuming $\zeta = -25$ mV, monovalent cation concentrations will be increased by 2.7 fold, anions decreased by 0.37 fold, and $Ca^{2+}/Mg^{2+}$ increased by 7.4 fold. As shown in Fig. 8, at low bath [Ca], both $Mg^{2+}$ and $K^+$ are present in filter with concentrations being 1.7 M and 7.7 M, respectively. As bath [Ca] increases, $Ca^{2+}$ would be selected to bind at filter. However, no difference was observed between neutral and charged membrane. One possible reason is that membrane potential would enhance all cation concentrations near the membrane simultaneously. Interestingly, we saw that the local electrostatic environment had almost no impact on the filter probabilities

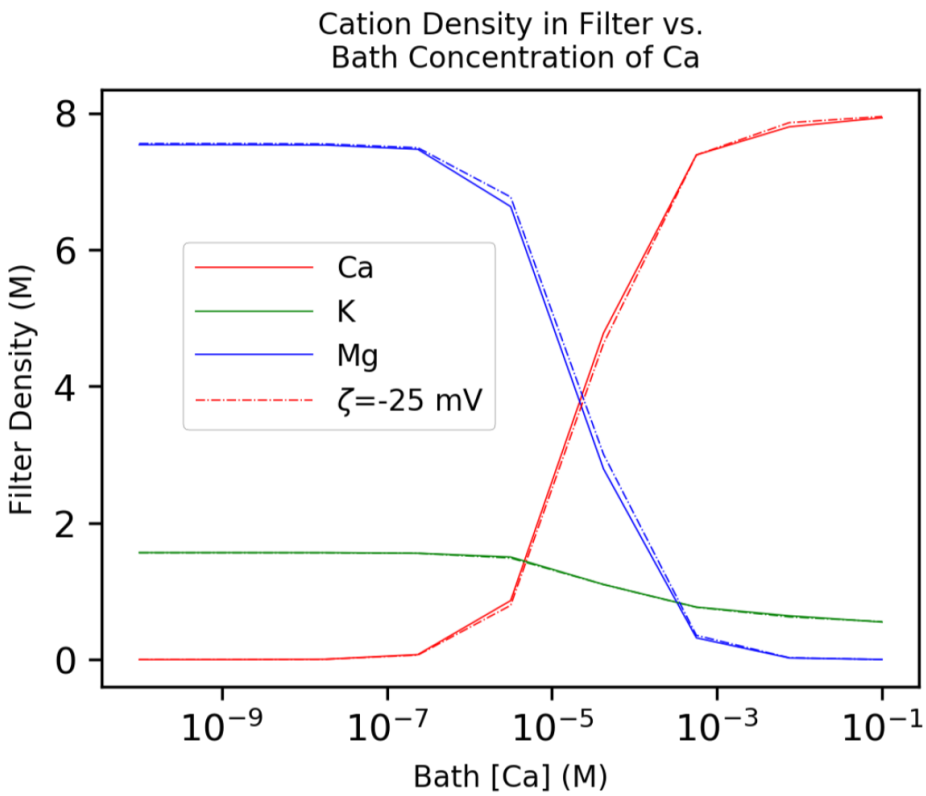


Figure 8: [figshort:fden]Filter cation density versus bath $Ca^{2+}$ concentration when filter volume = 0.33 $nm^3$ (volume of $Ca^{2+}$ binding sites derived from our MD simulations), $N_{oxy}$ = 7 (coordination number of $Ca^{2+}$ [27], this value lies between the coordination number of site I ($N_{oxy}$ = 8.5) and site II ($N_{oxy}$ = 6.7) $Ca^{2+}$ determined in our simulation of WT SERCA) and with the cation solvation energy from [30]. [KCl] = 150 mM and [$MgCl_2$] = 2 mM.

## 2.4 Steady-state catalytic activity

We first focus on $Ca_{only}$ in which only $Ca^{2+}$ is present in the model. The whole model consists of eight states (see $Ca_{only}$ in Fig. S4) and operates in the forward (clockwise) direction. In a whole cycle, two $Ca^{2+}$ ions in cytoplasm are transported into SR. For E1, a typical reaction ordering was proposed by Inesi et al [36] in which two $Ca^{2+}$ ions bind to SERCA through cooperative mechanism followed by the binding of MgATP. In this study, we proposed several state based description of this process, which we evaluate in terms of their ability to describe steady-state pump data.

In state model, except the transition rates between E1 and E2 ($k_5^+$, $k_5^-$, $k_6^+$ and $k_6^-$), the resting rate constants and substrate concentrations were taken from [36, 37]. The above four unknown rates were fitted so that $Ca_{only}$ model predicted SERCA turnover rate matches experimental data from [36]. During the fitting procedure, starting from initial guess values close to that in [36], the values of these four rate constants were adjusted until maximum alignment with experimental data achieved. As shown in Fig. 9, after fitting, the $Ca_{only}$ model predicted SERCA turnover rate curve excellently overlaps with experimental data. We further validated the state models with $Mg^{2+}$ and $K^+$ involved. In these models, the binding affinities of $Mg^{2+}/K^+$ to SERCA were taken either as experimental values in Table S4 or MSA predicted values or unphysically fitted values which enables maximum alignments between model predicted turnover rates and experimental data. The MSA predicted $Mg^{2+}/K^+$ potentials were first converted to dissociation constants via $K_d = e^{\frac{\mu_{MSA}}{RT}}$. The converted $K_d$ needs to be multiplied by a scaling factor $\lambda = 0.17$ to account for the difference between MSA predicted $Ca^{2+}$ dissociation constants and those from [36] (to determine $\lambda$, let $(Cai_{ref} - \lambda * Cai_{MSA})^2 - (Caii_{ref} - \lambda * Caii_{MSA})^2 = 0$, where $Cai_{ref}/Caii_{ref}$ and $Cai_{MSA}/Caii_{MSA}$ are site I/II $Ca^{2+}$ dissociation constants from [36] and from MSA calculations, respectively). As shown in Fig. 9(b-d), we note that the proposed models vary only in terms of their sensitivity to $Mg^{2+}/K^+$ binding, thus all should be similar at fixed [K] and [Mg]. The parameters used in our state models are listed in Table S3.

We further compared the turnover rates between WT and two variants with latter's $Ca^{2+}$ affinities adopted from MSA prediction. To be consistent with the procedure of obtaining $Mg^{2+}/K^+$ affinity from MSA potentials, the same scaling factor $\lambda = 0.17$ was also multiplied to $Ca^{2+}$ affinities of the E309Q and N796A variants.

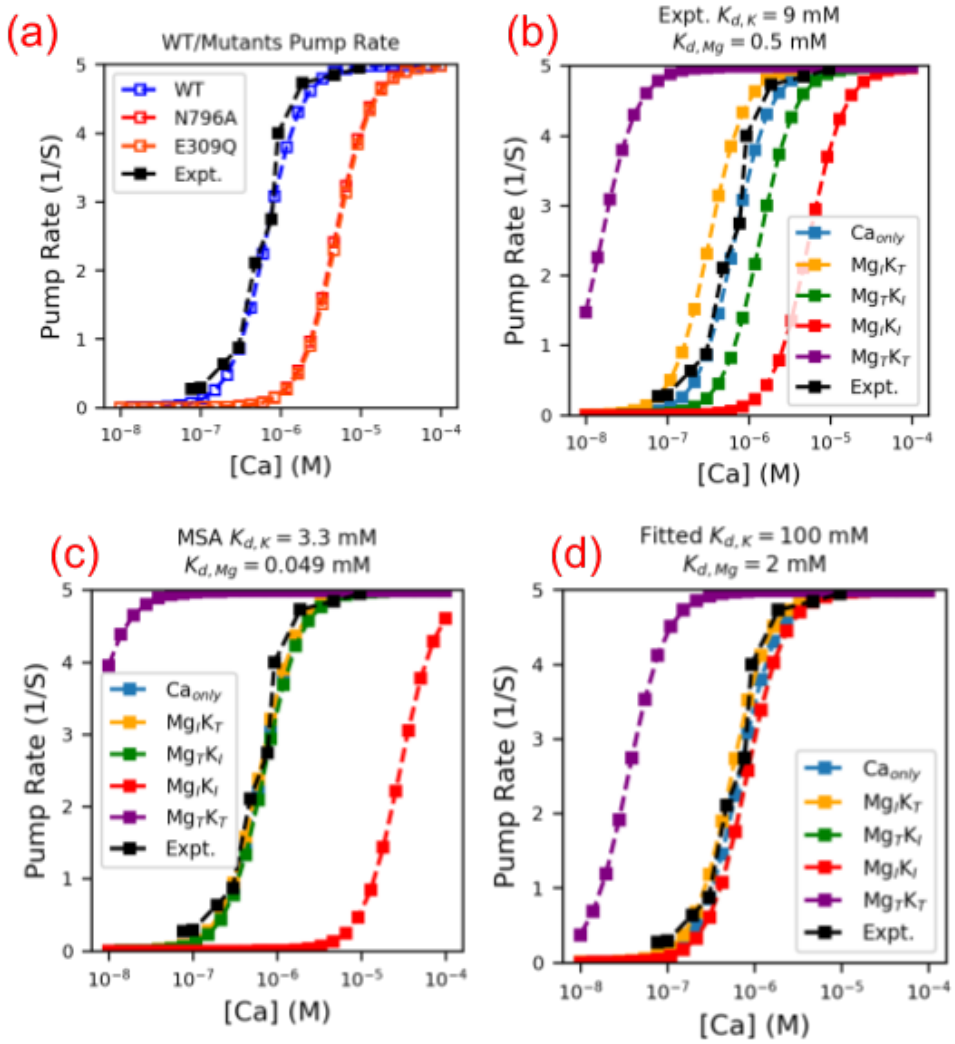


Figure 9: [figshort:turnover](a) Comparison of pump turnover rate between WT and SERCA variants using the $Ca_{only}$ model with MSA predicted $Ca^{2+}$ affinity for N796A and E309Q variants. The experimental data is from Inesi et al [36]. (b-d) Comparison of SERCA pump turnover rate of different state models against experimental data at [Mg] = 2 mM and [K] = 150 mM. In panel (b) the experimentally measured $K_{d,K}$ and $K_{d,Mg}$ in Table S4 were used. In panel (c) the MSA predicted $K_{d,K}$ and $K_{d,Mg}$ were used while in (d) fitted $K_{d,K}$ and $K_{d,Mg}$ were used to ensure maximum alignments of different models with experimental data.

As shown in Fig. 9, for WT SERCA, the $Ca_{only}$ model recaptures the [Ca] dependence of SERCA turnover rates and agrees with experimental data, as both of them reach the 2.5 $\frac{1}{s}$ half maximum rate when cytosolic [Ca] increased to about $1 \times 10^{-6}$ M. Compared to WT, the SERCA variants exhibit impaired pump rate activity as they reach half maximum rate at $\sim 1 \times 10^{-5}$ M [Ca], which is ten times as WT case. Here we demonstrated that by combining MSA predicted cation affinity and state model, we are able to offer quantitative description of experimentally observed SERCA activity decrease in E309Q and N796A variants [38]. MSA predicted affinities can then be used to rationalize steady-state pump and variants have attenuated pump turnover rates.

## 2.5 Effects on non-cognate ions on steady-state behavior of SERCA

The selectivity of $Ca^{2+}$-binding versus common endogenous cations, including $K^+$ and $Mg^{2+}$, is expected to influence the pump's apparent $Ca^{2+}$ affinity and turnover rate. To explore the effects of $Mg^{2+}/K^+$ on the steady-state behaviour, we calculated the [Ca] dependence of $Ca^{2+}$-binding to SERCA at varying [Mg] for different state models and compared against experimental data.

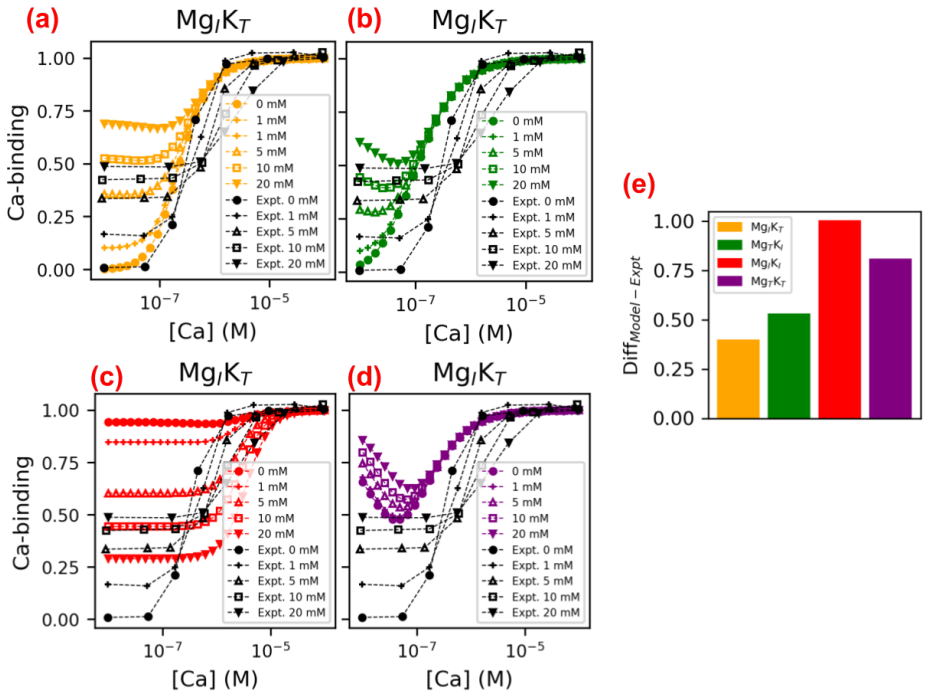


Figure 10: [figshort:cabind](a-d) Comparison of [Ca] dependence of $Ca^{2+}$-SERCA binding of different state models at varying $Mg^{2+}$ concentrations ([K]= 150 mM) against experimental data from [17] Experimentally measured $K_{d,K}$ and $K_{d,Mg}$ were used. (e) Normalized difference between each state model and experimental data for panels (d-g). $Diff = sqrt\left(\frac{\sum_{i=1}^{N}(M_{b,i}-Expt_{b,i})^2}{N}\right)$ where $M_{b,i}$ is state model predicted binding at experimental [Ca], $Expt_{b,i}$ is experimentally measured binding and $N$ is total number of data points.

Looking back, (b) and (c) panels in Fig. 9 together prove that, using either dissociation constant values for $Mg^{2+}/K^{+}$ from experiment or from MSA, $Mg_TK_T$ and $Mg_IK_I$ can be excluded as they deviate significantly from experimental data, while $Mg_IK_T$ and $Mg_TK_I$ are possible models as them are close to experimental data. Panel (c) shows that unphysically large dissociation constant values must be used if we force all models to align with experimental data, which indirectly support the conclusion obtained from (a) and (b). The data shown in Fig. 10(a-d) further help us to determine the most possible state model. The experimental data shown that Ca-SERCA binding increases with elevated [Mg]. This is because in experimental measurements, $Mg^{2+}$ was added into system prior to $Ca^{2+}$ and the formation of E1.Mg would cause the same fluorescence signaling as E1.2Ca. Thus experimentally measured $Ca^{2+}$ binding corresponds to the sum of E1.Mg and E1.2Ca. To be consistent with experiments, in our state models, we used the sum of E1.Mg and E1.2Ca probability as metric of Ca binding to SERCA. All four $Mg^{2+}/K^{+}$-containing state models recapture the trends exhibited in experimental data, albeit deviation exists. We calculated the difference between model and experimental data and inferred that $Mg_IK_T$ resembles experimental data most as indicated by the smallest normalized difference as 0.38. Hence we conclude that the most likely model is that $Mg^{2+}$ acts as inhibitor and $K^{+}$ as intermediate.

# 3 DISCUSSION

## 3.1 Ion coordination and contributions to cation binding affinity

A key contribution from this study was our use of MSA theory to evaluate trends in $Ca^{2+}$ and non-cognate binding in the SERCA E1 states. By using molecular dynamics simulations of the wild type and two site-directed mutations, we could probe shifts in the binding site configurations - relative to the available crystal structures of the pump - that contribute to chelating cations. Overall, the MSA theory, when informed using molecular simulation data including water distributions, appears to be effective in rank-ordering ions by affinity (approximately $-7$ to $-10$ kcal/mol, see Fig. 11).

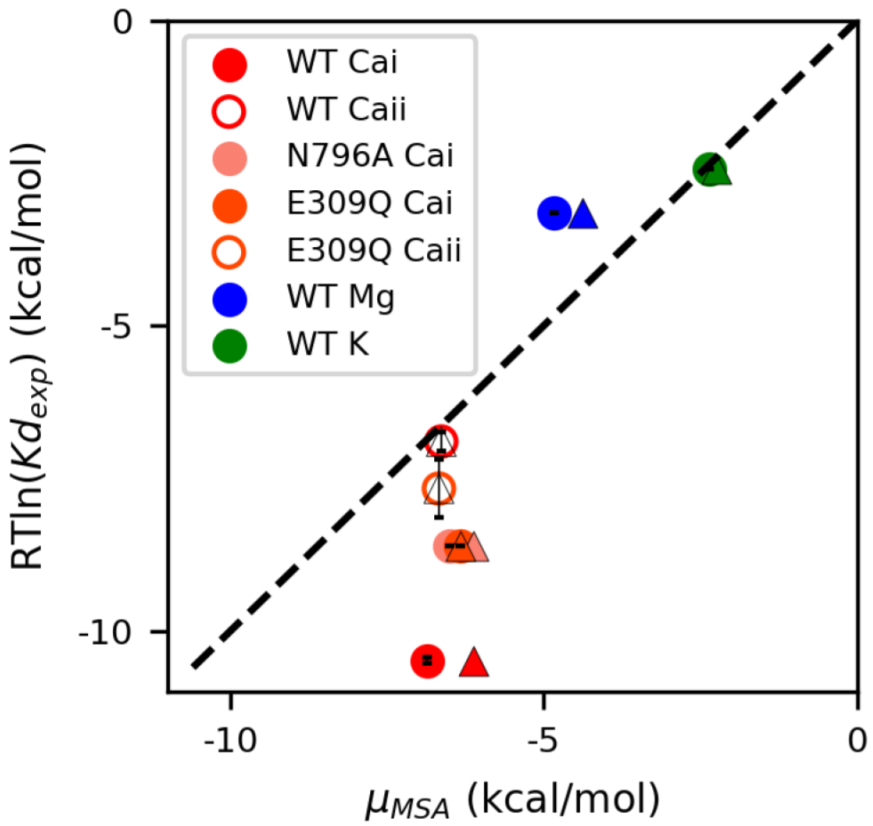


Figure 11: [figshort:expmsa]Correlation between MSA predicted chemical potential and experimentally measured binding free energy. The circles and triangles represent MSA results with waters and without waters taken into account, respectively. $RT$ = 0.593 kcal/mol at room temperature and $Kd_{exp}$ is experimentally measured dissociation constants in Table S4.

We first applied this combined MSA/MD technique to an EF-hand containing protein called $\beta$ parvalbumin to investigate factors contributing to its $Ca^{2+}$ affinity and selectivity [31]. In both systems, the MSA/MD approach indicated that high affinity $Ca^{2+}$ binding is afforded through the tight clustering of chelating oxygens with partial negative charges. Importantly, by predicting chemical potentials of ion binding, the MSA theory provides thermodynamic information about the relative competition between ions for the $Ca^{2+}$ binding domains, which is generally unfeasible by MD alone. For instance, we determined that $Mg^{2+}$, and not $K^{+}$, is thermodynamically more probable to occupy the pump at low $Ca^{2+}$ levels, but is disfavored as $Ca^{2+}$ rises toward micromolar concentrations typical in eukaryotic cells. In principle, this approach could additionally account for variations in electrolye composition expected near charged lipid bilayers, but we found scant differences in binding assuming a surface charge of 25 mV (see Fig. 8).

Consistent with our earlier findings for $Ca^{2+}$-binding to $\beta$ parvalbumin [31], MSA predicts increasing stability of the $Ca^{2+}$ ion as the number of coordinating oxygens is increased. This trend reverses as the oxygen density increases beyond roughly six per $2.2 \times 10^{-1}\,nm^3$, which is presumably when the volume is insufficient to accommodate all coordinating oxygens. For the E309Q and N796A variants, we potentially reduced the number of oxygens that could directly coordinate $Ca^{2+}$. Based on the MD simulations for E309Q, however, it appeared that the loss of one carboxylic acid oxygen was compensated for by forming a new interaction with E58 that maintained the same coordination number as the wild-type structure. This suggests that there is some degree of flexibility in coordination partners for the ion, which may facilitate the E309 residue's role in kinetically gating the binding site [20]. In contrast, the N796A mutation was not offset by a nearby available oxygen, thus the predicted chemical potential was less favorable. **Therefore, our data suggest that the MSA could reasonably rank-order $Ca^{2+}$ binding stabilities based on structures of the immediate coordination shell** based on Fig. 6, but it does not appear to capture the broad range of binding affinities reported in the literature (see Fig. 11).

We note that our predictions of favorable binding stabilities for $Ca^{2+}$ at site II for the N796A and E309Q variants are at odds with Inesi et al [39, 40], who suggested based on SERCA ATPase activity that the site was incapable of binding $Ca^{2+}$. Surprisingly, a structure of the E309Q variant (PDB ID: 4nab [15]) deposited in the protein databank contains $Ca^{2+}$ at both binding sites. Ostensibly, the E309Q variant has a much lower, but nonzero affinity for $Ca^{2+}$. Thus, it is likely that the MSA model does not sufficiently penalize nonoptimal $Ca^{2+}$ coordination, or reflect changes in internal strain that might disfavor coordination [31].

We found that including water distributions made a modest improvement in chemical potentials, as per Fig. 11. Based on Fig. S5, the narrow binding site volumes presented in sites I and II favor $Ca^{2+}$ and $Mg^{2+}$ over $K^{+}$, while both divalent ions are increasingly stabilized by greater densities of coordinating oxygens and waters. It is interesting that the water-free MSA calculations indicate $Ca^{2+}$ could be more stable in a binding site volume of $2.2 \times 10^{-1}\,nm^3$, which is

smaller than the volume presented in the MD simulations, albeit with a fewer number of oxygens (approximately five versus six). However, when water is considered, the stabilities at the smaller binding volumes are disfavored. It is possible that there is a kinetic advantage to having mobile waters involved in coordination, which could favor more rapid exchange of bound ions with the surrounding solvent. It is also possible that the trend can be explained on a thermodynamic basis, namely that by preserving waters that coordinate in the ion in bulk solvent, the desolvation cost upon binding SERCA are reduced, which should increase the apparent binding affinity. An intriguing possibility is that the $Ca^{2+}$ affinity could be indirectly tuned by controlling the density of binding site waters.

The primary function of the SERCA pump is to transport cytosolic $Ca^{2+}$ into the reticulum, therefore we verified that MSA would indeed predict an unfavorable change in chemical potential based on conformational changes induced in sites I and II upon forming the E2 state. Since the focus of this study was on the E1 $Ca^{2+}$ binding thermodynamics, we did not perform MD simulations of the E2 state. Based on the crystal structure of SERCA/beryllium fluoride complex(PDB ID: 3b9b [6]), which represents the pump's E2P state, we illustrate in Fig. 12 that drastic changes in the $Ca^{2+}$ binding site configuration, which culminate in a significant reduction in oxygens that could potentially coordinate $Ca^{2+}$. We further evaluate the binding stability for a hypothetical $Ca^{2+}$ bound between the labeled coordination groups and find that the MSA values are not only more positive than those of the E1 state, but are additionally greater than 0 kcal/mol. The positive values of approximately 1 kcal/mol indicate that $Ca^{2+}$ binding at these position is less thermodynamically favorable than partitioning into the surrounding bulk electrolyte. In other words, when SERCA transitions into the E2 state, it is thermodynamically preferred for $Ca^{2+}$ to vacate the binding site in favor of the reticulum lumen. Along these lines, mutations that alter the free energy difference for the $Ca^{2+}$ sites in the E1 and E2 configurations could affect the efficiency of the ATPase.

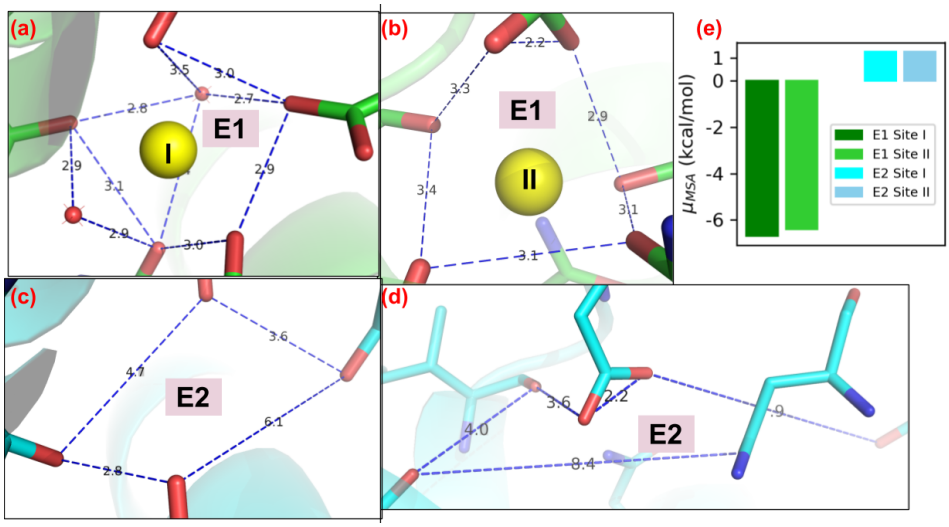


Figure 12: [figshort:e1e2] Comparison of $Ca^{2+}$ binding sites in E1 state (a-b) and E2 state (c-d) from crystal structures of PDB 1su4 and 3b9b [6], respectively. $Ca^{2+}$ and water molecules are shown as yellow and red spheres, respectively. The blue dashed lines in (a-b) outline the overall shape of $Ca^{2+}$ coordinating spheres in E1 state while in (c-d) they depict assumed $Ca^{2+}$ binding sites in E2 state. Panel (e) depicts MSA predicted $Ca^{2+}$ chemical potential for these two sites. In E1 state the number of coordinating oxygens are seven and six for site I and II while these values are assumed as four for both sites in E2 state.

It has been suggested that the number of cations ($Ca^{2+}$, $Mg^{2+}$, and $K^+$) bound to SERCA is approximately constant across its many conformational states [41]. In other words, $Ca^{2+}$ binding is offset by $Mg^{2+}$ and $K^+$ dissociation. ATP is bound to SERCA in complex with $Mg^{2+}$ [42], but there also exists structural [34] and activity [43] data that confirm $Mg^{2+}$ binds in the pump's transmembrane region. Toyoshima et al [34], for example, obtained the x-ray crystal structure of the pump with a single $Mg^{2+}$ bound at a 'hybrid' transmembrane site, for which the ion is coordinated by $\sim$5 oxygens with distances of approximately 2.0 Å. Since $Mg^{2+}$ bears the same charge as $Ca^{2+}$, but with a modestly smaller radius, it is somewhat surprising that $Mg^{2+}$ preferrentially binds at an intermediate site between the canonical $Ca^{2+}$ binding sites I and II. We attribute the thermodynamic preference for $Ca^{2+}$ at those sites based on two factors: the higher desolvation energy for $Mg^{2+}$ relative to $Ca^{2+}$ (779.94 kT vs 648.65 kT [44]) and the smaller binding site volume for the intermediate site versus sites I and II. With respect to the latter factor, in principle, $Mg^{2+}$ could reduce the site I and II volumes by pulling the chelating oxygens toward the smaller ion, as we previously observed in [31]. For the EF-hand (helix-loop-helix) containing protein, we found that reducing the binding loop region introduced greater strain for $Mg^{2+}$ relative to $Ca^{2+}$, which we suggested would reduce the overall binding affinity for $Mg^{2+}$. Although we did not explicitly evaluate strain that could be introduced upon $Mg^{2+}$-binding, we anticipate an even greater cost for reducing the binding site volume, since the chelating amino acid are firmly tethered to relatively immobile transmembrane helices. It is important to emphasize, though, that the non-optimal volumes for $Mg^{2+}$ binding at sites I and II does not preclude the ion from binding, as we demonstrate high binding probabilities at very low $Ca^{2+}$ levels (see Fig. 10).

Consistent with our earlier findings in $\beta$-PV, $K^+$ is disfavored from binding the native $Ca^{2+}$ binding volume based on its significantly larger radius and smaller charge [45]. However, $K^+$ and other monovalent cations have been demonstrated to stimulate SERCA function, with $K^+$ being the most efficient agonist [18, 41, 43]. Moreover, based on molecular simulations performed in the presence of transmembrane-bound $K^+$, Espinosa-Fonseca et al suggest that $K^+$ facilitates the pump's E2 to E1 transition through its stabilization of the E1 state [21] In our simulations, we found that of the two $K^+$ ions we placed in the $Ca^{2+}$ binding domains, the site I $K^+$ remained bound with approximately four coordinating oxygens with ion/oxygen distances exceeding 4 Å. Based on the MSA predictions, although $K^+$ does have a favorable ($\mu < 0$) binding potential that is consistent with its sub-millimolar binding affinity at site I [18], $Mg^{2+}$ and $Ca^{2+}$ are considerably more likely to be bound (see Fig. 8). Meanwhile, water frequently exchanged with $K^+$ in site II, which is suggestive of a low affinity for the cation.

Based on our comparison with proteins that selectively bind $K^+$, such as the KcsA $K^+$ channel, selective binding of $K^+$ over competing $Ca^{2+}$ might best be afforded through placement of carbonyl oxygens at sufficiently large distances to accommodate the $K^+$ ion. Namely, lining down the outer mouth of channel, oxygens from backbone or side chain of amino acid forming the

selectivity filter are exquisitely arranged to achieve precise pore size control (approximate diameter) and $K^+$-oxygen interaction strength [46]. In contrast, it is likely that $K^+$ exerts its agonistic effects on SERCA through binding the cytoplasmic domain, as was evidenced in a crystal structure determined by Sorenson et al, based on a bound $K^+$ ion in the P-domain [5]. According to the $K^+$-oxygen coordination pattern shown in Fig. S10, the MSA predicted potential for this P domain $K^+$ is $-2.38$ kcal/mol, which is comparable as $K^+$ in site I ($-2.35$ kcal/mol). Consistent with this structural evidence, the E2P.2Ca dephosphorylation data indicate that $K^+$ stimulates the $Ca^{2+}$-release step in this state, whereby the lumenal $Ca^{2+}$ affinity is reduced, rates of exchanging lumenal $Ca^{2+}$ with lumenal solvated $Ca^{2+}$ are accelerated [47], and $Ca^{2+}$ release is enhanced [48]. Similarly, dephosphorylation of the E2P state is blunted in the absence of $K^+$ [41].

Although the thermodynamics of $K^+$ binding are unfavorable relative to $Mg^{2+}$ and $Ca^{2+}$, there remains the possible role of $K^+$ in shaping the kinetics of SERCA function. It has been speculated, for instance, that $K^+$ accelerates $Ca^{2+}$ binding by first transiently occupying site I, after which it exchanges quickly with a $Ca^{2+}$ at site II [48]. $K^+$-facilitated exchange permits faster incorporation of $Ca^{2+}$ into site I, as opposed to the direct migration of $Ca^{2+}$ into a site that is potentially only partially-formed [48]. This interpretation is consistent with our observations from molecular dynamics simulations, and was initially reported in simulations of $Ca^{2+}$-free SERCAby Musgaard et al [49].

## 3.2 Relating cation affinity to ATPase activity

In our opinion, the bridging of molecular-level simulation and MSA thermodynamic data with state-based models represents a significant contribution toward multi-scale modeling of steady-state SERCA activity. Numerical and computational modeling of SERCA activity has spanned phenomenological frameworks, such as Hill-type models [50–52] to those representing distinct stages of the catalytic process as states [36, 37, 53–55]. Our implementation is based on the stepwise binding of $Ca^{2+}$ originally proposed by Inesi et al [36], but additionally considers $Mg^{2+}$- and $K^+$-bound states, followed by a reduction scheme to lump the E1 states separately from those comprising the E2 configurations. Significantly, the states defined in our model coincide with SERCA structures determined by x-ray crystallography and are ordered in a manner consistent with assays of SERCA function [56] In contrast, the state model proposed by Tran et al [37] assumed that ATP binding precedes the binding of two $Ca^{2+}$ ions, which has not been experimentally verified.

Existing models of SERCA function have faithfully recapitulated the pump's activity. However, an advantage of our state-based model is that its alignment with experimentally-determined structures permits us to directly investigate how structural modifications might impact activity. For example, we performed MSA/MD simulations of two mutated SERCA variants that yielded modified $Ca^{2+}$ binding constants that we used to predict SERCA activity (see Fig. 9).While we acknowledge that there are likely myriad changes to the pump's energetics following mutation that could be accounted for in the state-based model, our implementation here is a significant step toward structure-based

modeling of SERCA activity. At a minimum, our fitted state model is consistent with steady-state pump rates data collected as a function of $Ca^{2+}$ by Cantilina et al [36], $Ca^{2+}$-saturated versus $Mg^{2+}$ [17], as molecular simulations that predict $Mg^{2+}$ inhibition of the pump [21]. Furthermore, by considering different linkages of $K^+$- and $Mg^{2+}$-bound states to the reaction scheme, we were able to determine that assumptions of $Mg^{2+}$ inhibition and $K^+$ agonist were most consistent with experimental data collected by Guillain et al [17]. In principle, multiscale models of SERCA activity that include structure-derived thermodynamic information could permit in silico investigations of how disease-associated SERCA mutations [57, 58], post-translational modifications [59], and binding of regulatory proteins such as phospholamban [53] affect pump function.

## 3.3 Limitations

There are several limitations of our approach that could be addressed in future studies. Our study largely focused on conformational changes and energetics of the cations' immediate coordination sphere. $Mg^{2+}$ and $Ca^{2+}$-bound structures (PDB ID: 1su4 and 3w5b, respectively) deposited in the Protein Data Bank indicate substantial differences in the conformations of the transmembrane bundle helices and cytosolic domains that will necessarily contribute to the free energies of binding. For this reason, the free energy differences implied in experimental measurements of cation binding affinities reflect contributions from both ion coordination and the pump's different conformations. It is also important to emphasize that the MSA assumptions of a spherical binding volume within which amino acid oxygens are immobilized crudely approximates the actual binding site. Thus the predicted thermodynamic quantities are only appropriate for rank-ordering different ion/binding site configurations. Additionally, there is evidence [16, 56] that $Ca^{2+}$ binding is cooperative, although here we treat the binding events independently. It may be possible to partially recover some of the cooperative behavior by modeling SERCA with only one bound $Ca^{2+}$ and using end-point methods such as Molecular Mechanics/Poisson Boltzmann Surface Area (MM/PBSA) [60] to estimate energy changes upon binding a second $Ca^{2+}$. To our knowledge, however, a half-saturated $Ca^{2+}$-bound SERCA structure has not been determined, which would challenge efforts to validate predictions. Additionally, in the sequential binding model used by Inesi and others [6, 36] ($E1 \rightarrow E1.Ca \rightarrow E1'Ca \rightarrow E1'2Ca$), the apparent kinetics governing the transition between the E1.Ca to E1'Ca states can vary depending on a variety of factors, including the presence the regulatory protein phospholamban [53, 61]. Thus, extending this model to broader conditions and regulatory proteins would require careful consideration of conformational changes that might accompany the E1.Ca to E1'Ca transition. Lastly, the $Ca^{2+}$-binding steps in our model are assumed to be in steady state relative to the substantially slower transitions between the E1 and E2 states. In the event that the pump is subject to rapid $Ca^{2+}$ oscillations, such as spontaneous $Ca^{2+}$ spiking in glia [62], the steady-state approximation may be unreliable.

# 4 CONCLUSIONS

We utilized molecular dynamics simulations, mean sphere approximation theory and state-based modeling to probe effects of $Ca^{2+}$, $Mg^{2+}$ and $K^+$ binding on the SERCA pump cycle. The MD and MSA approaches indicate that favorable binding of $Ca^{2+}$ in the wild-type SERCA configuration is facilitated through a high degree of coordination by amino acid comprising the binding sites, as well as significant contributions of water coordination. This coordination pattern appears to be impaired in the E309Q and N796A variants; using MSA theory, we found that the chemical potential of $Ca^{2+}$ binding is reduced (ANK:increased since binding is impaired?) relative to wild-type as a result. Hence, mutations near the $Ca^{2+}$ binding domains that alter the coordination number, hydration and binding site volume can be expected to modulate $Ca^{2+}$ affinity in a manner qualitatively described by the MSA theory. Similarly, the coordination patterns exhibited in the $Mg^{2+}$ and $K^+$-bound structures led to less favorable binding estimated from MSA-theory. These findings were qualitatively consistent with measured affinity data reported in the literature [15–18, 39, 48]. Additionally, we developed a state-based model of SERCA activity that we used to: 1) relate $Ca^{2+}$ binding affinities to the SERCA pump rate; and 2) determine whether $Mg^{2+}$ and $K^+$ are pump agonists or inhibitors. We found that the state model treating $Mg^{2+}$ as an inhibitor and $K^+$ as an agonist ($Mg_I K_T$) was most consistent with experimental data. Despite the limitations of the assumptions used for the various models, we believe that the approach provides an attractive framework for evaluating allosteric functional effects of ion binding on SERCA, which may be extendable to other $Ca^{2+}$ transporters, such as P2X4 [63].

# 5 METHODS

## 5.1 Construction of the SERCA systems

Molecular dynamics (MD) simulations on wild-type (WT) SERCA and two variants of SERCA: E309Q and N796A were performed; the latter variants were chosen given dimished site II $Ca^{2+}$-binding [38]. For the WT SERCA system, we considered apo, $Ca^{2+}$-bound, $Mg^{2+}$-bound and $K^+$-bound states. $Ca^{2+}$-bound (PDB ID: 1su4 [3]) and $Mg^{2+}$-bound (E1.Mg, PDB ID: 3w5b [34]) SERCA X-ray crystal structures were used as the starting structures. The apo SERCA system was constructed based on 1su4 with two $Ca^{2+}$ ions removed as done in [64]. The structure of the site I or II bound $K^+$ SERCA has not been determined, thus we created the structure based on the $Mg^{2+}$-bound variant . For the N796A mutant, $Ca^{2+}$-bound and $Mg^{2+}$-bound cases were considered, based on mutating N796 to alanine. Similarly, for the E309Q mutant, we obtained two rotamers compatible with the binding site as evaluated through UCSF Chimera [65]. These E309Q rotamers were designated as "E309Q_r1" and "E309Q_r2". All SERCA cases considered in present study are summarized in Table S1.

The cation coordinating acidic residues E309, E771 and D800 were assumed to be deprotonated, while E908 was protonated, consistent with [21]; further a

disulfide bond was introduced between residues C876 and C888. The system was inserted into a homogeneous 1-palmitoyl-2-oleoyl-*sn*-glycero-3-phosphocholine (POPC) lipid bilayer of POPC via the Membrane Builder [66] within the CHARMM-GUI software [67]. This system was solvated via TIP3P waters [68] using a 20 Å margin perpendicular to the membrane. Counterions $K^+$ and chloride ($Cl^-$) were added into the system via Monte-Carlo method to neutralize the system and maintain an ionic strength of 0.15 M. Both the solvation and ion-adding were performed via the Solvator module within CHARMM-GUI online-server. The final system contained ∼255,000 atoms including lipid bilayer with 461 lipids, and ∼59,000 TIP3P water molecules and was parameterized by the CHARMM36 force field [69, 70].

## 5.2 Molecular dynamics simulations

MD simulations were performed using NAMD [71]. The system was first subjected to an energy minimization process consisting of 2000 steps' steepest descent (SD) and 2000 steps' adopted basis Newton rRphson (ABNR) algorithm. For each case, the minimized system was heated from 0 K to 303.14 K over 25 ps with 1 fs timestep via the Langevin thermostat, using randomized velocities for three triplicate preparations. For each replica, harmonic constraints were introduced during minimization and heating on protein side chains, protein backbone atoms, lipid heavy atoms and ions. The force constants of constraints were set to 5, 10, 10 and $1.0 \times 10^1 \frac{k}{\text{mol Å}^2}$, respectively, and were gradually reduced to zero over five equilibration steps of 20 ps in duration. 100 ns production simulations was then performed on the equilibrated system with the Shake algorithm [72], using 2 fs timesteps.

## 5.3 Simulation trajectory analysis

Standard trajectory analyses including RMSF and coordination oxygen/$Ca^{2+}$ distances were computed using Lightweight Object-Oriented Structure Library (LOOS) [73]. Coordination pattern analysis on each cation with oxygen atoms from nearby amino acids were performed in each binding site. This consisted of extracting residues within 20 Å from D800 (the shared residue of the conventional two $Ca^{2+}$-binding sites in SERCA) based on the $Ca^{2+}$-bound SERCA crystal structure (PDB ID: 1su4). The water density around cation was computed via the radial command implemented in CPPTRAJ [74] and analyzed via GIST (as described below).

The MSA is a mean-field model which estimates cation chemical potentials in electrolyte solution with finite-sized ions. In this study, the SERCA cation binding sites were treated as confined filters filled with oxygens from coordinating residues and water molecules. The MSA model calculates cation distributions between bulk electrolyte solution that minimize the chemical potential for partitioning ions into a finite size volume occupied by coordinating oxygens; these volume and number of oxygens were determined by MD as in Kucharski et al[31]. The free energy expression in this model was assuming negative-charged spherical domains was based on a chemical potential accounting for electrostatic and hard-sphere interactions between ions inclusive

of oxygens, as described in [32, 75, 76]. In this representation, which is analogous to the $Ca^{2+}$ binding domain in $\beta$-PV and calcium channels [30–32], ionic species that have a negative chemical potential in the binding filter are thermodynamically favored to bind. We include in this approach a solvation contribution as estimated via generalized Born theory of ion hydration energies:

$$\Delta G_{GB} = \frac{z^2}{r}\left(\frac{e^2 N_a}{2 \cdot 4\pi\epsilon_0}\right)\left(1 - \frac{1}{\epsilon_r}\right) \tag{1}$$

where $z$ is charge number, $r$ is radii, $e$ is electron charge, $N_a$ is the Avogadro constant, $\epsilon_0$ and $\epsilon_r$ are vacuum dielectric and the relative dielectric constant of the solvent. Additional details are elaborated in the supplementary material of [31]

In the SERCA system, the cation/SERCA configurations can present differing numbers of coordination oxygen atoms (see Fig. 4 and Table S2) and volumes, as shown previously for $\beta$-PV in [31]:

$$V_f = \frac{4}{3}\pi R^3 \tag{2}$$

$$R = r_{rdf} + r_{oxy} \tag{3}$$

where $r_{rdf}$ is the radii of optimal coordination sphere which can be obtained from the cation-oxygen coordination pattern analysis based on MD simulations (see Fig. 4) while $r_{oxy}$ is the radii of oxygen atom. Charges and radii values of all ions are taken from the Li-Merz work [77]. The specific parameters used in the MSA calculations are listed in Table S2.

## 5.4 Grid Inhomogeneous Solvation Method (GIST)

The GIST model [78, 79] was used to characterize the theromodynamic properties of coordinating water. GIST calculations were performed via the SSTmap program [80]. Before GIST calculations, the MD trajectory was first subjected to rms fitting on key cation coordinating residues to align cation binding sites. The C$\alpha$ atoms of residues V304, I307, N768, E771, N796 and D800 were used for this rms fitting. The grid center required in GIST was defined by the cation coordinates obtained from the last frame in the rms-fitted trajectory. Grid dimensions were set to 16, 20 and 20 with grid spacing being 0.5 Å. The free energy of water at each grid point was calculated as $\Delta G = E_{sw} + E_{ww} - dTS_{orient} - dTS_{trans}$ where $E_{sw}$ and $E_{ww}$ are solute-water and water-water interaction energies while $dTS_{orient}$ and $dTS_{trans}$ are orientational and translational entropic energies.

## 5.5 State-based model of SERCA pump cycle

SERCA pumping is characterized by two prominent states: E1 and E2. In the E1 state, two $Ca^{2+}$ ions bind to SERCA through cooperative mechanism followed by the binding of MgATP [36]. We represent each state as by an ordinary differential equation of the form

$$ds_i/dt = \sum k_{ji} s_j - \sum k_{ij} s_i \tag{4}$$

where $s_i$ is state i, and $k_{ij}$ describe rates for transitioning between states i and j. The models tested in this paper are summarized in Fig. S4 . While the cooperative $Ca^{2+}$ binding mechanism in the E1 state is well-accepted, the $Ca^{2+}$ release mechanism of the E2 state is not clearly resolved, therefore we use the state represntations proposed in Tran et al [37].

Based on the technique proposed by Smith et al [81], we can apply rapid equilibrium assumption to fast processes (those within E1 or E2) relative to the slow rates of transitions between the E1 and E2 states to simplify the model. As shown in Fig. S4, states in dashed boxes were assumed to be in quasi-steady-state and thus can be lumped together. Hence, the original multi-state models could be simplified into a two-state model (see bottom Fig. S4) in which new apparent rate constants were derived based on original rate constants. The resulting equations are summarized in the supplement Sect. S1.4.

For the lumped 2-state model, the turn over rate is derived as in Tran's paper [37]:

$$V = \frac{\alpha_1^+\alpha_2^+ - \alpha_1^-\alpha_2^-}{\alpha_1^+ + \alpha_1^- + \alpha_2^+ + \alpha_2^-} \tag{5}$$

where $\alpha_i^{\pm}$ are apparent rate constants between lumped two states (the expressions are given in Sect. S1.4). The final parameters used in present work are listed in Table S3.

# 6 ACKNOWLEDGEMENT

Research reported in this publication was supported by the Maximizing Investigators' Research Award (MIRA) (R35) from the National Institute of General Medical Sciences (NIGMS) of the National Institutes of Health (NIH) under grant number R35GM124977, as well as the award 1F32HL114365-01A1. This work used the Extreme Science and Engineering Discovery Environment (XSEDE), which is supported by National Science Foundation grant number ACI-1548562. We thank Seth Robia and Michael Autry for discussion of this work.

# S1 Supplementary Information (SI): Cation binding to SERCA

B Sun, BD Stewart, AN Kucharski, PM Kekenes-Huskey*
Department of Chemistry, University of Kentucky, 505 Rose St.
Chemistry-Physics Building, Lexington, KY, USA 40506
* Corresponding authors. E-mail address: pkekeneshuskey@uky.edu (P. Kekenes-Huskey)

## S1.1 Supplementary Tables

Table S1: MD simulation cases

| Cases | Cation occupancy | PDBID of ini. struc | Simulation length (ns) |
|---|---|---|---|
| WT | 2 $Ca^{2+}$s | 1su4 | 300 |
| WT | 1 $Mg^{2+}$ | 3w5b | 300 |
| WT | 2 $K^{+}$s | 3w5b | 300 |
| N796A | 2 $Ca^{2+}$s | 1su4 | 400 |
| N796A | 1 $Mg^{2+}$s | 3w5b | 355 |
| E309Q_r1[a] | 2 $Ca^{2+}$s | 1su4 | 240 |
| E309Q_r2[b] | 2 $Ca^{2+}$s | 1su4 | 170 |

[a,b]Different rotamers of Q309 side chain

## S1.2 Supplementary Figures

Table S2: Parameters used in SERCA MSA model. The diameter and charge of ions were adapt from Li-Merz work [77] and the solvation energy for ions were taken from table 1 in Nonner et al [30].

| Parameter | Definition | Values |
|---|---|---|
| $N_{oxy}$ at $Ca^{2+}$ site I | no. of amino acid oxygen | 5.5 |
| $N_{oxy}$ at $Ca^{2+}$ site II | no. of amino acid oxygen | 6.7 |
| $N_{oxy}$ at $K^{+}$ site I | no. of amino acid oxygen | 3.9 |
| $N_{oxy}$ at $Mg^{2+}$ site | no. of amino acid oxygen | 4.2 |
| $r_{rdf}$ at $Ca^{2+}$ site I, II | optimal coordination radii | 2.5 Å |
| $r_{rdf}$ at $Mg^{2+}$ site | optimal coordination radii | 2.0 Å |
| $r_{rdf}$ at $K^{+}$ site I | optimal coordination radii | 2.9 Å |
| $\rho_i$ | Bath [KCl] | 150 mM |
| | bath [$MgCl_2$] | 1 mM |
| | bath [$CaCl_2$] | 0.1 nM to 0.1 M |
| $\epsilon_f$ | filter dielectric | 25.0 |
| $\epsilon_b$ | bath dielectric | 78.4 |
| $\sigma_O$ | O diameter | 0.354 nm |
| $\sigma_{Ca}$ | $Ca^{2+}$ diameter | 0.272 nm |
| $\sigma_{Mg}$ | $Mg^{2+}$ diameter | 0.236 nm |
| $\sigma_K$ | $K^{+}$ diameter | 0.352 nm |
| $\sigma_{Cl}$ | $Cl^{-}$ diameter | 0.454 nm |
| $z_O$ | O charge | -0.7469 e |
| $z_{Ca}$ | $Ca^{2+}$ charge | 1.77 e |
| $z_{Mg}$ | $Mg^{2+}$ charge | 1.69 e |
| $z_K$ | $K^{+}$ charge | 1 e |
| $z_{Cl}$ | $Cl^{-}$ charge | -1 e |
| $w_{Ca}$ | solvation energy | -648.65 kT [44] |
| $w_{Mg}$ | solvation energy | -779.94 kT [44] |
| $w_K$ | solvation energy | -141.59 kT [44] |
| $w_{Cl}$ | solvation energy | -122.63 kT [44] |
| kT/zF | | 25.6 mV |
| $V_f$ of $Ca^{2+}$ sites | filter volume | 0.326 $nm^3$ |
| $V_f$ of $Mg^{2+}$ site | filter volume | 0.224 $nm^3$ |
| $V_f$ of $K^{+}$ site I | filter volume | 0.426 $nm^3$ |

Table S3: Parameters used SERCA state-based model models in present work.

| Parameter | Value | reference |
|---|---|---|
| $K_{d,Mg}$ | $2 \times 10^{-3}$ M/$5 \times 10^{-4}$ M | fitted/Expt. |
| $K_{d,K}$ | $1 \times 10^{-1}$ M/$9 \times 10^{-3}$ M | fitted/Expt. |
| $K_{d,2}$ | $2.24 \times 10^{-3}$ M | [37] |
| Ca(SR) | $1 \times 10^{-6}$ M | [36] |
| [MgATP] | $3 \times 10^{-4}$ M | [36] |
| [MgADP] | $1 \times 10^{-6}$ M | [36] |
| [Pi] | $1 \times 10^{-6}$ M | [36] |
| $k_1^+$ | $1 \times 10^8 \frac{1}{s}$ | [36] |
| $k_1^-$ | $4 \times 10^2 \frac{1}{s}$ | [36] |
| $k_2^+$ | $3.0 \times 10^1 \frac{1}{s}$ | [36] |
| $k_2^-$ | $4.0 \times 10^1 \frac{1}{s}$ | [36] |
| $k_3^+$ | $4 \times 10^8 \frac{1}{s}$ | [36] |
| $k_3^-$ | $1.6 \times 10^1 \frac{1}{s}$ | [36] |
| $k_4^+$ | $2 \times 10^7 \frac{1}{s}$ | [36] |
| $k_4^-$ | $4.0 \times 10^1 \frac{1}{s}$ | [36] |
| $k_5^+$ | $1.5 \times 10^1 \frac{1}{s}$ | fitted |
| $k_5^-$ | $7.5 \frac{1}{s}$ | fitted |
| $k_6^+$ | $7.5 \frac{1}{s}$ | fitted |
| $k_6^-$ | $7 \times 10^9 \frac{1}{s}$ | fitted |

Table S4: Experimental dissociation constant of cations with SERCA

| Cation | Dissociation constant ($K_d$) | reference |
|---|---|---|
| $Ca^{2+}$ site I | 0.018 - 0.023 $\mu$M | [16] |
| $Ca^{2+}$ site II | 6.67 - 11.1 $\mu$M | [16] |
| $Mg^{2+}$ | 5 mM / 0.5 mM[a] | [17] and [48] |
| $K^+$ site I | 0.625 mM | [18] |
| $K^+$ site II | 16.67 mM | [18] |
| $K^+$ binds to P-domain[b] | na | [5] |
| N796A and E309Q $Ca^{2+}$ site I | 0.5 $\mu$M | [39] |
| N796A and E309Q $Ca^{2+}$ site II | no binding | [39] |
| E309Q with 2 $Ca^{2+}$ binding | 0.46 - 4.38 $\mu$M[c] | [15] |

[a] in [48] it was postulated that $Mg^{2+}$ binds to site II with $K_d$ = 0.5 mM and this bound-$Mg^{2+}$ would exchange quickly with $Ca^{2+}$ and the consequence is $Mg^{2+}$ accelerates $Ca^{2+}$ bindings to SERCA; [b] a $K^+$ binding site located in P-domain was identified via X-ray crystallography; [c] This data is apparent affinity for both site I and II obtained by fitting to experimental data using Hill equation.

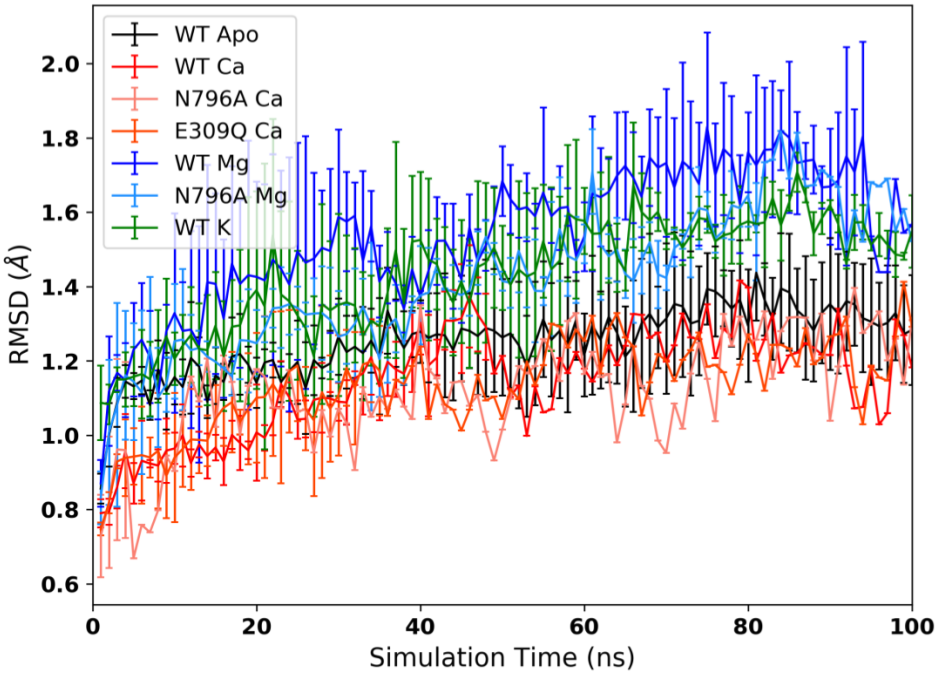


Figure S1: [figshort:tmrmsd]Back-bone atom RMSD of TM helices vs. simulations time. The error bars are calculated from the triplicate trajectories for each case.

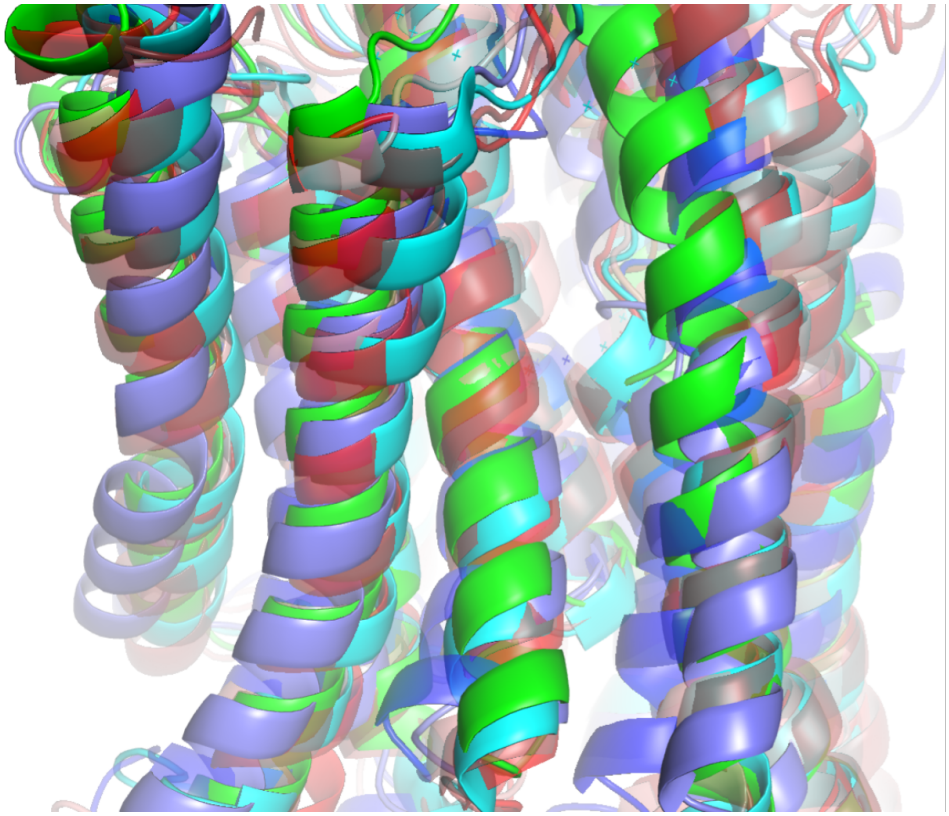

Figure S2: [figshort:tmoverlap]TM alignments of MD-simulated structures to x-ray crystal structures of PDB 1su4. The MD-simulated structures are extracted from MD trajectories at 80 ns and colored as red for $Ca^{2+}$-bound cases, blue for $Mg^{2+}$-bound cases and green for $K^{+}$-bound cases. The crystal structure is colored in cyan.

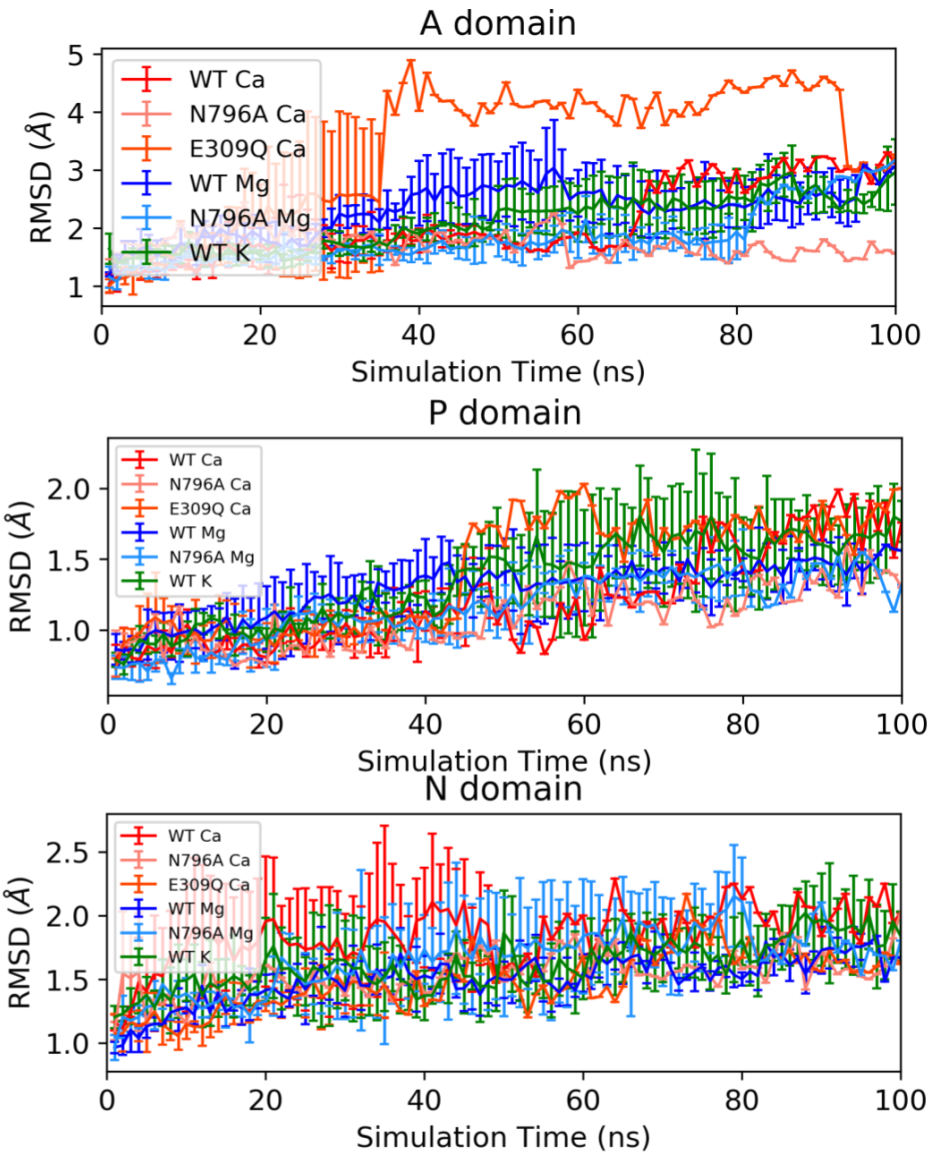


Figure S3: [figshort:cytormsd]Back-bone atom RMSD of cytosolic domains vs. simulations time. Alignments were conducted using backbone atoms of cytosolic domains. The error bars are calculated from the triplicate trajectories for each case.

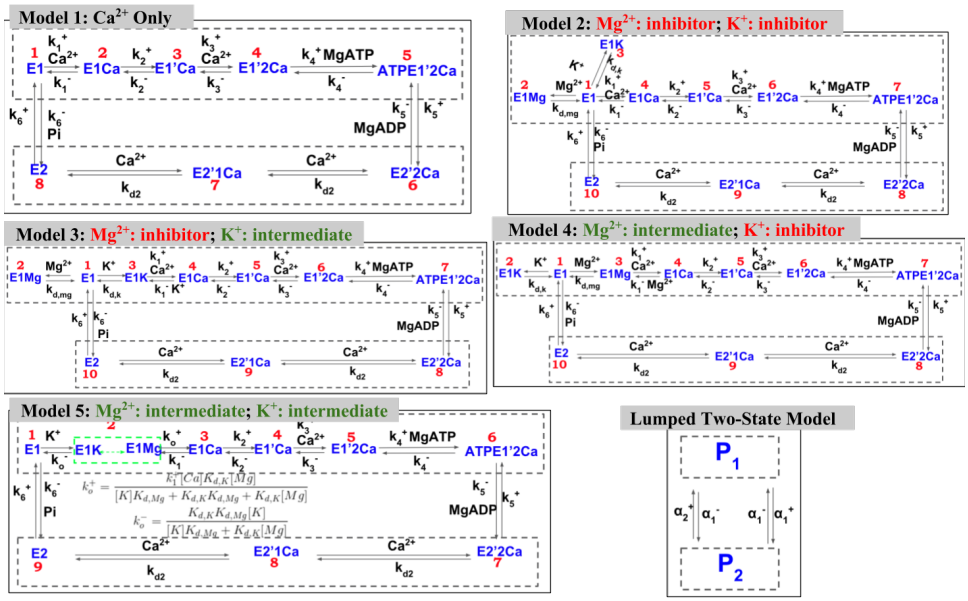


Figure S4: [figshort:msmmodels]Schema of the five state-based model models of SERCA pump considered in present study. In Model 1 ($Ca_{only}$), only the native $Ca^{2+}$ cation is involved in the pump cycle. In Model 2 ($Mg_I K_I$), both $Mg^{2+}$ and $K^+$ are assumed to act as inhibitors of SERCA. In Model 3 ($Mg_I K_T$), $Mg^{2+}$ is assumed to act as inhibitors of SERCA while $K^+$ acts as intermediate. In Model 4 ($Mg_T K_I$), the roles of $Mg^{2+}$ and $K^+$ are opposite as Model 3, namely, $Mg^{2+}$ is assumed to act as intermediate of SERCA while $K^+$ acts as inhibitor. In Model 5 ($Mg_T K_T$), both $Mg^{2+}$ and $K^+$ are assumed to act as intermediates of SERCA. For all models, the states in dashed-box are lumped together based on the lumping strategy proposed by Smith et al [81] to form a two-state model. The apparent rates between the two-state model are given in supplementary material.

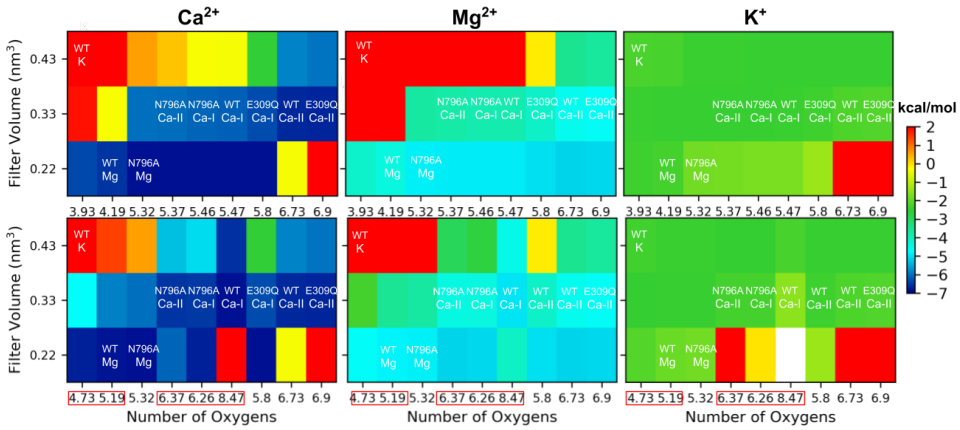


Figure S5: [figshort:excessen]Chemical potential of cation in the filter calculated via MSA at various values of filter volume ($V_f$) and coordinated oxygens. The upper and lower row represent results where coordinating water molecules were excluded and included, respectively. The red boxed xticks in lower row highlighted the total number of coordinating oxygens when water were take into account. The bath ionic strength are [KCl] = 150 mM, [$MgCl_2$] = 2 mM and [$Ca^{2+}$]= 1 $\mu$M. The three filter volumes of the $y$-axis are optimal volumes for $Ca^{2+}$ (0.33 $nm^3$), $Mg^{2+}$ (0.22 $nm^3$) and $K^+$ (0.43 $nm^3$). The values at $x$-axis correspond to the optimal coordinating oxygens determined from MD simulations.

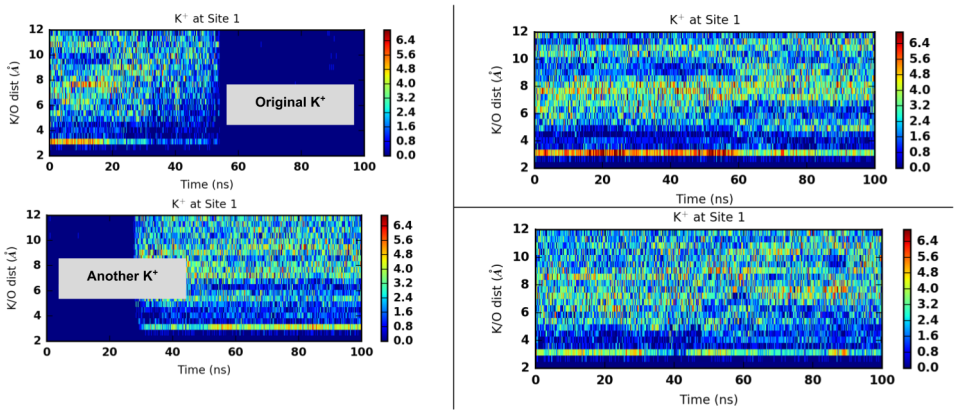


Figure S6: [figshort:wtktime]Coordination pattern of $K^+$ at SERCA site I with residue oxygen atoms in the 1st 100 ns WT simulations. In the 1st 100 ns simulation, the original $K^+$ at site I flee away after about 40 ns, however, another $K^+$ will bind at site I afterwards. The radial distribution is calculated based on the second $K^+$ after 40 ns.

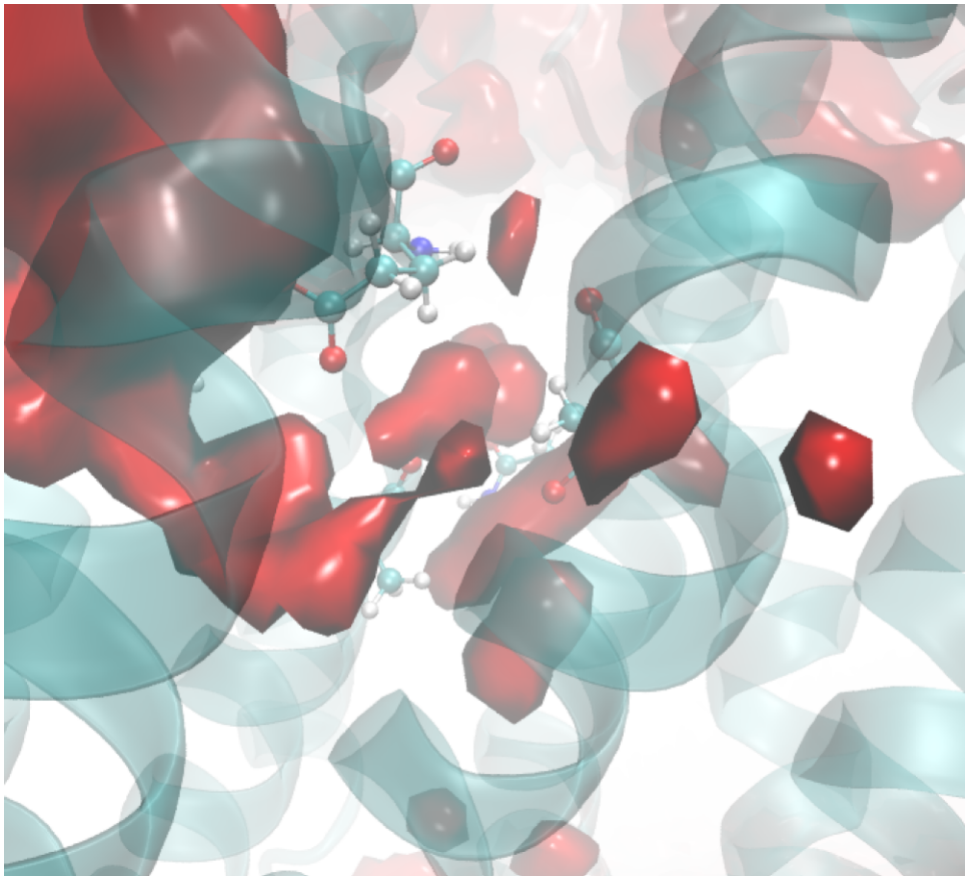

Figure S7: [figshort:apowat]Water density in $Ca^{2+}$ binding sites calculated from apo SERCA MD simulations via the VolMap module of VMD. The key coordinating residues are shown as sticks. The shown red isosurface depicts water density as 0.35.

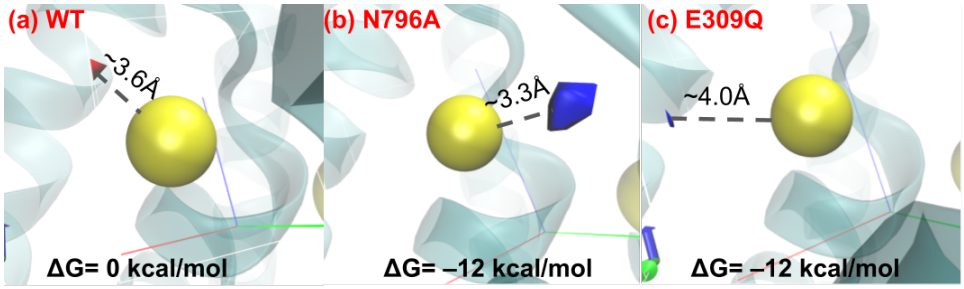


Figure S8: [figshort:site2cagist]Free energy of water sites around site II $Ca^{2+}$ calculated by GIST. For N796A and E309Q, the blue isosurface corresponds to water sites with $\Delta G = -12$ kcal/mol. For WT the shown red isosurface depicts a water oxygen density as 0.075 while the $\Delta G$ is 0 everywhere over the grids. The distance between $Ca^{2+}$ and isosurface is also shown.

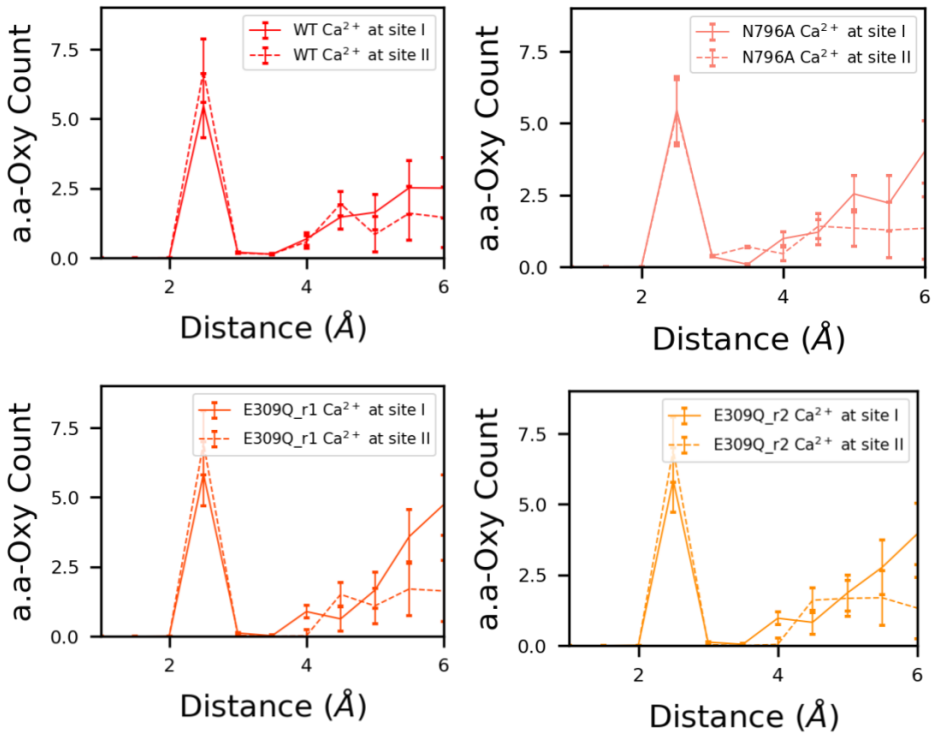


Figure S9: [figshort:caspec]Radial distribution of oxygen around $Ca^{2+}$ for each case.

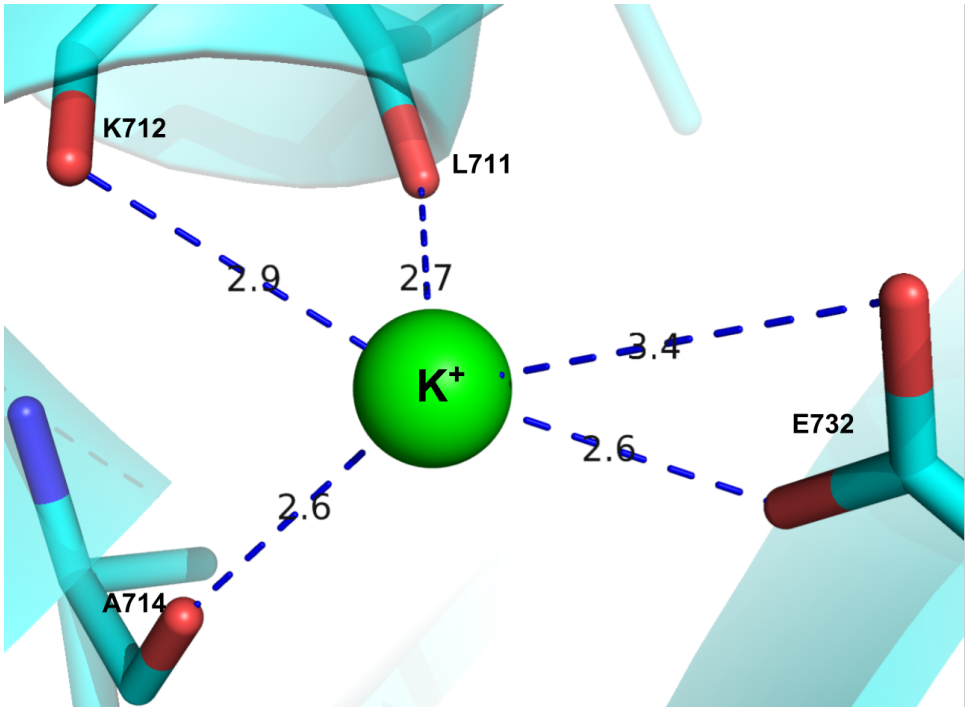


Figure S10: [figshort:pK]$K^+$ binding site at P domain from crystal structure PDB 1t5s. Number of coordinating oxygens is five and filter volume is assumed to be 0.43 $nm^3$.

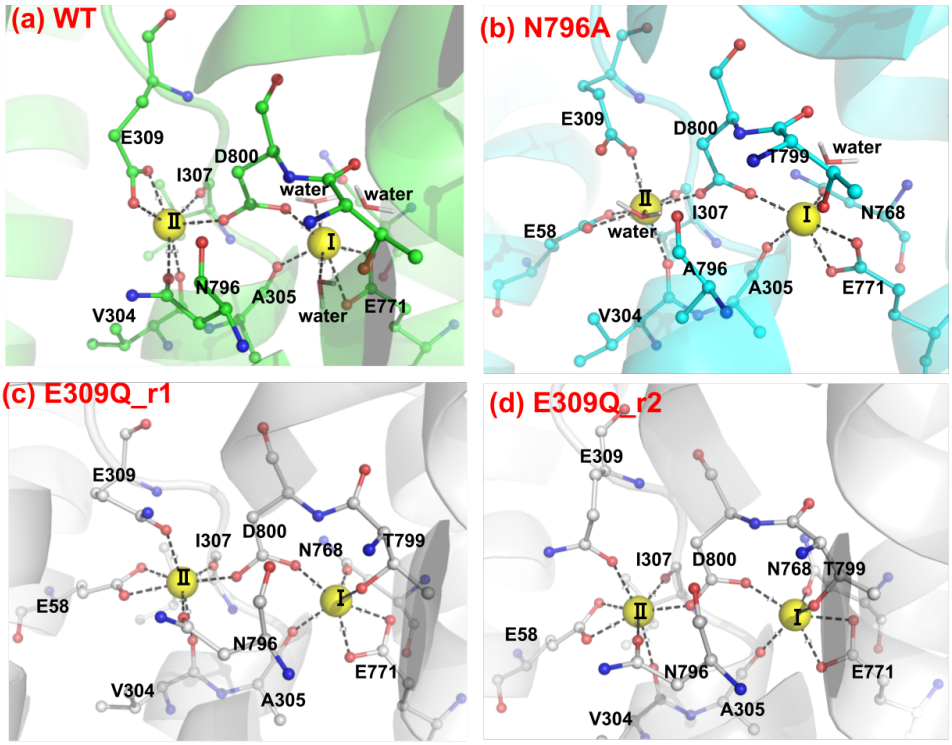


Figure S11: [figshort:cacoor]Representative coordination patterns of $Ca^{2+}$ (yellow spheres) in the two binding sites from MD simulation in WT SERCA and mutants. Key residues are shown in sticks and balls. In WT site I, there are 3 waters coordinating with $Ca^{2+}$, while in N796A/E309Q mutants, site I $Ca^{2+}$ has one/zero coordinating water molecules.

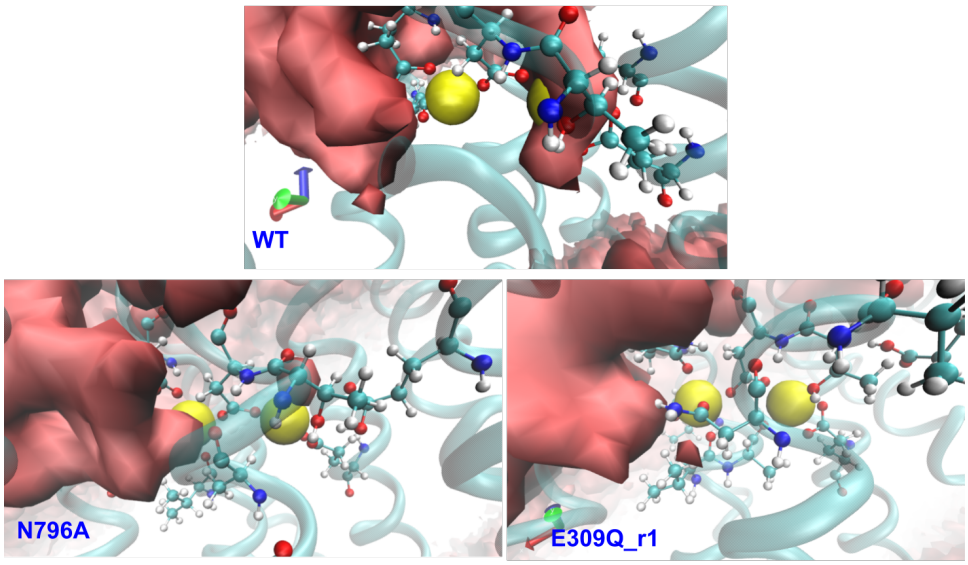


Figure S12: [figshort:watden]Water density around $Ca^{2+}$ (yellow spheres) calculated from MD simulations via the VolMap module of VMD. The shown red isosurface depicts water density as 0.2.

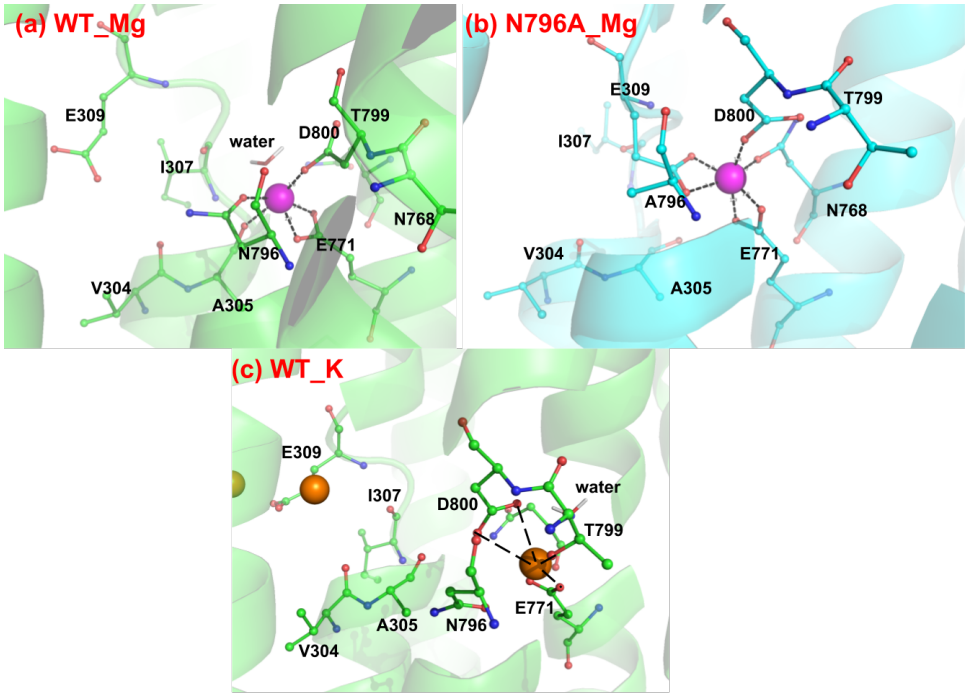


Figure S13: [figshort:mgkcoor]Representative coordination patterns of $Mg^{2+}$ (magenta spheres) and $K^{+}$ (orange spheres) in the binding sites from MD simulation in WT SERCA and mutants. In both WT and N796A, $Mg^{2+}$ resides in a 'hybrid' binding site rather than the conventional two $Ca^{2+}$ binding site. $K^{+}$ at site I is stable and not stable $K^{+}$ binds at site II.

## S1.3 Supplementary Methods

Here we summarize our lumping strategy used to simply SERCA model. Often in the kinetic models for enzyme activity, if there are processes occur on timescales which are much faster than others in the model, we can reduce the complexity by lumping these fast processes together. We will use the lumping strategy proposed by Smith et al [81] to simply our SERCA models. The basic ideal of this strategy can be clearly illustrated by a general example as following:

```
          k1+     k2+     k3+
...S1<---->S2<--->S3<--->S4....
          k1-     k2-     k3-
```

S1 to S4 are four states with forward and reverse rate constants connecting neighboring states. Suppose S2 and S3 are in rapid equilibrium with each other, namely $k_2^+$,$k_2^- >> k_1^+$,$k_1^-$,$k_3^+$,$k_2^-$. At any time:

$$S3(t) = K_2 * S2(t) \tag{S1}$$

$$K_2 = \frac{k_2^+}{k_2^-} \tag{S2}$$

Now we lump S2 and S3 together to form a new pseudo state S23. For the lumped model, we will use new apparent rate constants $\alpha_1^+$, $\alpha_1^-$, $\alpha_2^+$, $\alpha_2^-$ to represent the transition between states.

```
                 ---------
          a1+ |   k2+   | a2+
...S1<---->|S2<--->S3|<--->S4....
          a1- |__ k2-___| a2-
                 S23
```

For the lumped model, we have:

$$S23(t) = S2(t) + S3(t) \tag{S3}$$

$$= (1 + K_2)S2(t) \tag{S4}$$

$$= (1 + \frac{1}{K_2})S3(t) \tag{S5}$$

$$S2(t) = \frac{1}{1 + K_2} S23(t) \tag{S6}$$

$$S3(t) = (1 + \frac{1}{K_2})S23(t) \tag{S7}$$

Now we consider relationship between original rate constants and the new apparent rate constants. In both models, for S4, we have:

$$S4(t) = S3(t)k_3^+ = S23(t)\alpha_2^+ \tag{S8}$$

Now we put Eq(7) into Eq(8), we see clearly that:

$$\frac{k_3^+}{1 + \frac{1}{K_2}} S23(t) = S23(t)\alpha_2^+ \tag{S9}$$

so we have the expression of $\alpha_2^+$ as:

$$\alpha_2^+ = \frac{k_3^+}{1 + \frac{1}{K_2}} \tag{S10}$$

similarly, we can derive the expression of $\alpha_1^+$, $\alpha_1^-$, $\alpha_2^-$:

$$\alpha_1^+ = k_1^+ \tag{S11}$$

$$\alpha_1^- = \frac{k_1^-}{1 + K_2} \tag{S12}$$

$$\alpha_2^- = k_3^- \tag{S13}$$

$$\frac{dP_{1-5}}{dt} = -(\alpha_2^- + \alpha_1^+)P_{1-5} + (\alpha_2^+ + \alpha_1^-)P_{6-8} \tag{S14}$$

$$V_{max} = \frac{\alpha_1^+\alpha_2^+ - \alpha_1^-\alpha_2^-}{\alpha_1^+ + \alpha_1^- + \alpha_2^+ + \alpha_2^-} \tag{S15}$$

$$I_{Ca2+} \propto N_{SERCA} V_{max} \tag{S16}$$

## S1.4 Apparent rate constants between lumped two-state model.

For $Ca_{only}$ model, the apparent rate constants are:

$$\begin{aligned}
\alpha_1^+ &= \frac{k_5^+ K1K2K3K4[Ca]_i^2[MgATP]}{1 + K1[Ca]_i + K1K2[Ca]_i + K1K2K3[Ca]_i^2 + K1K2K3K4[Ca]_i^2[MgATP]} \\
\alpha_1^- &= \frac{k_5^-[MgADP]}{1 + \frac{K_{d2}}{[Ca]_{sr}} + \frac{K_{d2}^2}{[Ca]_{sr}^2}} \\
\alpha_2^+ &= \frac{k_6^+}{1 + \frac{[Ca]_{sr}^2}{K_{d2}^2} + \frac{[Ca]_{sr}}{K_{d2}}} \\
\alpha_2^- &= \frac{k_6^-[Pi]}{1 + K1[Ca]_i + K1K2[Ca]_i + K1K2K3[Ca]_i^2 + K1K2K3K4[Ca]_i^2[MgATP]}
\end{aligned} \tag{S17}$$

where $Ki = \frac{k_i^+}{k_i^-}$ $(i = 1, 2, 3, 4)$ and the value for each parameter is listed in Table S3. For models with $Mg^{2+}/K^+$ involved, the apparent rate constants can be expressed via the general expression Eq. S18:

$$\begin{aligned}
\alpha_1^+ &= \frac{k_5^+ \phi_1\phi_2 K1K2K3K4[Ca]_i^2[MgATP]}{1 + \phi_1 + \phi_1\phi_2 + \phi_1\phi_2 K1[Ca]_i + \phi_1\phi_2 K1K2[Ca]_i + \phi_1\phi_2 K1K2K3[Ca]_i^2 + \phi_1\phi_2 K1K2K3K4[Ca]_i^2[MgATP]} \\
\alpha_1^- &= \frac{k_5^-[MgADP]}{1 + \frac{K_{d2}}{[Ca]_{sr}} + \frac{K_{d2}^2}{[Ca]_{sr}^2}} \\
\alpha_2^+ &= \frac{k_6^+}{1 + \frac{[Ca]_{sr}^2}{K_{d2}^2} + \frac{[Ca]_{sr}}{K_{d2}}} \\
\alpha_2^- &= \frac{k_6^-[Pi]}{1 + \phi_1 + \phi_1\phi_2 + \phi_1\phi_2 K1[Ca]_i + \phi_1\phi_2 K1K2[Ca]_i + \phi_1\phi_2 K1K2K3[Ca]_i^2 + \phi_1\phi_2 K1K2K3K4[Ca]_i^2[MgATP]}
\end{aligned} \tag{S18}$$

The expression of $\phi_1$ and $\phi_2$ differs in different models. For $Mg_IK_I$, we have:

$$\begin{aligned}
\phi_1 &= \frac{K_{d,Mg}}{[Mg]} \\
\phi_2 &= \frac{K_{d,K}}{[K]}
\end{aligned} \tag{S19}$$

For $Mg_IK_T$, we have:

$$\begin{aligned}
\phi_1 &= \frac{K_{d,Mg}}{[Mg]} \\
\phi_2 &= \frac{[K]}{K_{d,K}}
\end{aligned} \tag{S20}$$

For $Mg_TK_I$, we have:

$$\phi_1 = \frac{K_{d,K}}{[K]}$$
$$\phi_2 = \frac{[Mg]}{K_{d,Mg}} \tag{S21}$$

For $Mg_TK_T$, we have:

$$\phi_1 = \frac{[K]([K]K_{d,Mg} + [Mg]K_{d,K})}{K_{d,K}[K]K_{d,Mg}}$$
$$\phi_2 = \frac{k_1^+[Ca]K_{d,K}[Mg]}{([K]K_{d,Mg} + K_{d,K}K_{d,Mg} + K_{d,K}[Mg])k_1^-[Mg]} \tag{S22}$$

## S1.5 Supplementary results

As shown in Table S5, the cations in the simulation maintained most of coordinating amino acid found in crystal structure with few exceptions. In the crystal structure, site I $Ca^{2+}$ has five coordinating amino acid oxygens within 2.5 Å. In our simulations, site I $Ca^{2+}$ lost coordination with the N768 $O_{\delta 1}$ atom (4.82 Å) and the coordination with T799 $O_{\gamma 1}$ also presented larger distances (3.46 $\pm$ 0.92 Å). However, the site I $Ca^{2+}$ also gained two new coordinating amino acid oxygens with E771 $O_{\delta 2}$ and A305 O at 2.20 and 2.27 Å, respectively. The net effect is that site I $Ca^{2+}$ in simulation has slightly larger number of amino acid oxygen than WT (5.5 vs 5), as indicated in Fig. 4. Interestingly, in simulations site I $Ca^{2+}$ also gained one more coordinating water when compared with crystal structure, making the number of coordinating waters reaching three. These waters were stabilized via hydrogen bonds with neighbouring oxygens, e.g., backbone oxygen of E908, N768 and the side chain oxygen of T799.

Meanwhile, the site II $Ca^{2+}$ lost one coordination pairing with E309 $O_{\epsilon 2}$ as the distance became 3.43 Å compared with 2.63 Å in crystal structure, whereas the ion established a bidentate coordination with E58. We note that the standard deviation between E58 $O_{\epsilon 2}$ atom and $Ca^{2+}$ is 0.60 Å, which is about six fold higher than the other positions, which indicated that E58 coordination is highly dynamic in comparison. For the E309Q and N796A variants, the number of coordinating amino acid oxygens to cations are comparable with the WT case but coordinating water density are significantly smaller (see inserted bar graphs in Fig. 4). Site II $Ca^{2+}$ preserved coordination reflected in crystal structure. Similarly, $Mg^{2+}$ lost coordination with A305 O but gain coordination with D800 $O_{\delta 2}$ and therefore maintained same coordination number as crystal structure.

At the time of this study, to our knowledge there is no experimentally-determined structural information of SERCA with $K^+$ bound at transmembrane sites, however, it has been reported that $K^+$ binds to site I with sub-millimolar affinity [18]. In this study we show that the initially $K^+$ placed at binding site II is unstable and exchange frequently with $K^+$ ions in solvent at a sub-100 ns timescale while $K^+$ at site I is stable as shown in Fig. S6.

Table S5: Distance between cation and coordinating amino acid oxygens in Å.

| amino acid oxygen | $Cai_{crystal}$ | $Cai_{WT}$ | $Caii_{crystal}$ | $Caii_{WT}$ | $Mg_{crystal}$ | $Mg_{WT}$ |
|---|---|---|---|---|---|---|
| T799 $O_{\gamma 1}$ | 2.36 | $3.46 \pm 0.92$ | | | | |
| E771 $O_{\epsilon 1}$ | | $2.20 \pm 0.09$ | | | 2.50 | $1.89 \pm 0.06$ |
| E771 $O_{\epsilon 2}$ | 2.39 | $2.19 \pm 0.09$ | | | 1.86 | $1.87 \pm 0.05$ |
| D800 $O_{\delta 1}$ | 2.38 | $2.11 \pm 0.05$ | | $4.29 \pm 0.09$ | | $3.74 \pm 0.13$ |
| D800 $O_{\delta 2}$ | | $3.75 \pm 0.19$ | 2.34 | $2.15 \pm 0.06$ | | $1.80 \pm 0.04$ |
| A305 O | | $2.27 \pm 0.10$ | | | 2.63 | $4.06 \pm 0.19$ |
| N768 $O_{\delta 1}$ | 2.33 | $4.82 \pm 1.37$ | | | 2.31 | $2.03 \pm 0.09$ |
| E908 $O_{\epsilon 1}$ | 2.44 | | | | | |
| I307 O | | | 2.32 | $2.30 \pm 0.09$ | | |
| V304 O | | | 2.40 | $2.32 \pm 0.09$ | | |
| N796 $O_{\delta 1}$ | | | 2.22 | $2.25 \pm 0.07$ | 2.62 | $1.99 \pm 0.08$ |
| E309 $O_{\epsilon 1}$ | | | 2.37 | $2.23 \pm 0.43$ | | |
| E309 $O_{\epsilon 2}$ | | | 2.63 | $3.43 \pm 0.69$ | | |
| E58 $O_{\epsilon 1}$ | | | | $2.27 \pm 0.29$ | | |
| E58 $O_{\epsilon 2}$ | | | | $2.48 \pm 0.60$ | | |
| $No_{total}$ | 5.0 | 5.5 | 6.0 | 6.7 | 5.0 | 4.2 |

In the simulations, $K^+$ at site I forms three stable coordination pairs with E771 $O_{\epsilon 1}$, $O_{\epsilon 2}$ atoms and T799 $O_{\gamma 1}$ atom at around 3.0 Å and a highly dynamic coordination with D800 $O_{\delta 2}$ atom ($3.99 \pm 1.80$ Å) as indicated by the large standard deviation, therefore yielding a total number of coordinating amino acid oxygens of approximately 3.9. We conclude that the MD simulations concur with the experimentally-resolved coordination patterns, although the identity of the coordinating residues present an appreciable degree of variability. We later relate these coordination pattern to binding potential.

# References


[1] H. Ma, G. Inesi, and C. Toyoshima. "Substrate-induced conformational fit and headpiece closure in the Ca2+ ATPase (SERCA)". In: *Journal of Biological Chemistry* 278.31 (Aug. 2003), pp. 28938–28943. ISSN: 00219258.

[2] G. Inesi, A. M. Prasad, and R. Pilankatta. "The Ca2+ATPase of cardiac sarcoplasmic reticulum: Physiological role and relevance to diseases". In: *Biochemical and Biophysical Research Communications* 369.1 (2008), pp. 182–187. ISSN: 0006291X. arXiv: NIHMS150003.

[3] C. Toyoshima et al. "Crystal structure of the calcium pump of sarcoplasmic reticulum at 2.6 A resolution". In: *Nature* 405.6787 (2000), pp. 647–655. ISSN: 0028-0836.

[4] C. Toyoshima and H. Nomura. "Structural changes in the calcium pump accompanying the dissociation of calcium". In: *Nature* 418.6898 (Aug. 2002), pp. 605–611. ISSN: 00280836.

[5] T. L. M. Sørensen et al. "Localization of a K+-binding site involved in dephosphorylation of the sarcoplasmic reticulum Ca2+-ATPase". In: *Journal of Biological Chemistry* 279.45 (Nov. 2004), pp. 46355–46358. ISSN: 00219258.

[6] C. Olesen et al. "The structural basis of calcium transport by the calcium pump". In: *Nature* 450.7172 (Dec. 2007), pp. 1036–1042. ISSN: 14764687.

[7] G. Inesi and A. Scarpa. "Fast kinetics of adenosine triphosphate dependent Ca 2+ uptake by fragmented sarcoplasmic reticulum". In: *Biochemistry* 11.3 (Feb. 1972), pp. 356–359. ISSN: 0006-2960.

[8] J. P. Froehlich and E. W. Taylor. "Transient state kinetic effects of calcium ion on sarcoplasmic reticulum adenosine triphosphatase". In: *Journal of Biological Chemistry* 251.8 (Mar. 1976), pp. 2307–2315. ISSN: 00219258.

[9] Y. Dupont. "Fluorescence studies of the sarcoplasmic reticulum calcium pump." In: *Biochemical and biophysical research communications* 71.2 (July 1976), pp. 544–50. ISSN: 0006-291X.

[10] Y. Dupont and J. B. Leigh. "Transient kinetics of sarcoplasmic reticulum Ca2++Mg2+ATPase studied by fluorescence". In: *Nature* 273.5661 (June 1978), pp. 396–398. ISSN: 00280836.

[11] C. R. Coan and G. Inesi. "Ca2+-dependent effect of acetylphosphate on spin-labeled sarcoplasmic reticulum." In: *Biochemical and biophysical research communications* 71.4 (Aug. 1976), pp. 1283–8. ISSN: 0006-291X.

[12] L. Meis and A. L. Vianna. "Energy Interconversion by the Ca2+-Dependent ATPase of the Sarcoplasmic Reticulum". In: *Annual Review of Biochemistry* 48.1 (1979). PMID: 157714, pp. 275–292. eprint: https://doi.org/10.1146/annurev.bi.48.070179.001423.

[13] G. Inesi. "Mechanism of Calcium Transport". In: *Annual Review of Physiology* 47.1 (1985). PMID: 2581506, pp. 573–601. eprint: https://doi.org/10.1146/annurev.ph.47.030185.003041.

[14] E. Mintz and F. Guillain. "Ca2+ transport by the sarcoplasmic reticulum ATPase". In: *Biochimica et Biophysica Acta (BBA) - Bioenergetics* 1318.1 (1997), pp. 52–70. ISSN: 0005-2728.

[15] J. D. Clausen et al. "SERCA mutant E309Q binds two Ca 2+ ions but adopts a catalytically incompetent conformation". In: *EMBO Journal* 32.24 (Dec. 2013), pp. 3231–3243. ISSN: 02614189.

[16] G. Inesi et al. "Cooperative calcium binding and ATPase activation in sarcoplasmic reticulum vesicles." In: *Journal of Biological Chemistry* 255.7 (Apr. 1980), pp. 3025–3031.

[17] F. Guillain, M. P. Gingold, and P. Champeil. "Direct fluorescence measurements of Mg2+ binding to sarcoplasmic reticulum ATPase." In: *Journal of Biological Chemistry* 257.13 (July 1982), pp. 7366–7371. ISSN: 00219258.

[18] a. G. Lee et al. "Effects of K+ on the binding of Ca2+ to the Ca(2+)-ATPase of sarcoplasmic reticulum." In: *The Biochemical journal* 305 ( Pt 1 (Jan. 1995), pp. 225–31. ISSN: 0264-6021.

[19] Y. Huang, H. Li, and Y. Bu. "Molecular dynamics simulation exploration of cooperative migration mechanism of calcium ions in sarcoplasmic reticulum Ca2+-ATPase". In: *Journal of Computational Chemistry* 30.13 (Oct. 2009), pp. 2136–2145. ISSN: 01928651. arXiv: NIHMS150003.

[20] P. M. Kekenes-Huskey et al. "Calcium binding and allosteric signaling mechanisms for the sarcoplasmic reticulum Ca2+ ATPase". In: *Protein Science* 21.10 (2012), pp. 1429–1443. ISSN: 1469-896X.

[21] L. M. Espinoza-Fonseca, J. M. Autry, and D. D. Thomas. "Microsecond molecular dynamics simulations of Mg2+- And K+- Bound E1 intermediate states of the calcium pump". In: *PLoS ONE* 9.4 (2014). ISSN: 19326203.

[22] A. Das et al. "Conformational Transitions and Alternating-Access Mechanism in the Sarcoplasmic Reticulum Calcium Pump". In: *Journal of Molecular Biology* 429.5 (2017), pp. 647–666. ISSN: 10898638.

[23] H. Rui et al. *Proton Countertransport and Coupled Gating in the Sarcoplasmic Reticulum Calcium Pump*. 2018.

[24] K. N. Ha et al. "Lethal Arg9Cys phospholamban mutation hinders Ca2+-ATPase regulation and phosphorylation by protein kinase A". In: *Proceedings of the National Academy of Sciences* 108.7 (2011), pp. 2735–2740. ISSN: 0027-8424.

[25] P. Bidwell et al. "Phospholamban binds with differential affinity to calcium pump conformers". In: *Journal of Biological Chemistry* 286.40 (Oct. 2011), pp. 35044–35050. ISSN: 00219258.

[26] N. Smolin and S. L. Robia. "A structural mechanism for calcium transporter headpiece closure". In: *Journal of Physical Chemistry B* 119.4 (Jan. 2015), pp. 1407–1415. ISSN: 15205207.

[27] T. Dudev and C. Lim. *Competition among metal ions for protein binding sites: Determinants of metal ion selectivity in proteins*. Jan. 2014.

[28] H. Yu, S. Y. Noskov, and B. Roux. "Two mechanisms of ion selectivity in protein binding sites". In: *Proceedings of the National Academy of Sciences* 107.47 (Nov. 2010), pp. 20329–20334. ISSN: 00223476. arXiv: 15334406.

[29] Y. Kiyota and M. Takeda-Shitaka. "Molecular recognition study on the binding of calcium to calbindin D9kbased on 3D reference interaction site model theory". In: *Journal of Physical Chemistry B* 118.39 (Oct. 2014), pp. 11496–11503. ISSN: 15205207.

[30] W. Nonner et al. "Ion accumulation in a biological calcium channel: Effects of solvent and confining pressure". In: *Journal of Physical Chemistry B* 105.27 (2001), pp. 6427–6436. ISSN: 10895647.

[31] A. N. Kucharski et al. "Understanding Ion Binding Affinity and Selectivity in -Parvalbumin Using Molecular Dynamics and Mean Spherical Approximation Theory". In: *The Journal of Physical Chemistry B* 120.33 (2016), pp. 8617–8630.

[32] W. Nonner, L. Catacuzzeno, and B. Eisenberg. "Binding and selectivity in L-type calcium channels: a mean spherical approximation." In: *Biophysical journal* 79.4 (2000), pp. 1976–1992. ISSN: 0006-3495.

[33] D. Gillespie et al. "A physical mechanism for large-ion selectivity of ion channels". In: *Physical Chemistry Chemical Physics* 4.19 (Sept. 2002), pp. 4763–4769. ISSN: 14639076.

[34] C. Toyoshima et al. "Crystal structures of the calcium pump and sarcolipin in the Mg 21 -bound E1 state". In: *Nature* 495 (2013).

[35] E. Hughes, J. C. Clayton, and D. A. Middleton. "Cytoplasmic residues of phospholamban interact with membrane surfaces in the presence of SERCA: A new role for phospholipids in the regulation of cardiac calcium cycling?" In: *Biochimica et Biophysica Acta (BBA) - Biomembranes* 1788.2 (2009), pp. 559–566. ISSN: 0005-2736.

[36] T. Cantilina et al. *Comparative studies of cardiac and skeletal sarcoplasmic reticulum ATPases: Effect of a phospholamban antibody on enzyme activation by Ca2+*. 1993.

[37] K. Tran et al. "A thermodynamic model of the cardiac sarcoplasmic/endoplasmic Ca2+(SERCA) pump". In: *Biophysical Journal* 96.5 (2009), pp. 2029–2042. ISSN: 15420086.

[38] D. M. Clarke et al. "Location of high affinity Ca2 +-binding sites within the predicted transmembrahe domain of the sarco-plasmic reticulum Ca2+-ATPase". In: *Nature* 339.6224 (June 1989), pp. 476–478. ISSN: 00280836.

[39] G. Inesi, Z. Zhang, and D. Lewis. "Cooperative setting for long-range linkage of Ca2+binding and ATP synthesis in the Ca2+ATPase". In: *Biophysical Journal* 83.5 (Nov. 2002), pp. 2327–2332. ISSN: 00063495.

[40] G. Inesi et al. "Ca2+ occlusion and gating function of Glu309 in the ADP-fluoroaluminate analog of the Ca2+-ATPase phosphoenzyme intermediate". In: *Journal of Biological Chemistry* 279.30 (July 2004), pp. 31629–31637. ISSN: 00219258.

[41] M. Shigekawa and L. J. Pearl. "Activation of calcium transport in skeletal muscle sarcoplasmic reticulum by monovalent cations." In: *The Journal of biological chemistry* 251.22 (Nov. 1976), pp. 6947–52. ISSN: 0021-9258.

[42] A. L. Vianna. "Interaction of calcium and magnesium in activating and inhibiting the nucleoside triphosphatase of sarcoplasmic reticulum vesicles". In: *Biochimica et Biophysica Acta (BBA) - Enzymology* 410.2 (1975), pp. 389–406. ISSN: 0005-2744.

[43] L. R. Jones. "Mg2+and ATP effects on K+activation of the Ca2+-transport ATpase of cardiac sarcoplasmic reticulum". In: *BBA - Biomembranes* 557.1 (Oct. 1979), pp. 230–242. ISSN: 00052736.

[44] W. R. Fawcett. "Thermodynamic Parameters for the Solvation of Monatomic Ions in Water". In: *The Journal of Physical Chemistry B* 103.50 (1999), pp. 11181–11185. eprint: `https://doi.org/10.1021/jp991802n`.

[45] R. D. Shannon and C. T. Prewitt. "Effective ionic radii in oxides and fluorides". In: *Acta Crystallographica Section B* 25.5 (May 1969), pp. 925–946.

[46] J. F. Cordero-Morales et al. "Molecular determinants of gating at the potassium-channel selectivity filter". In: *Nature Structural and Molecular Biology* 13.4 (Apr. 2006), pp. 311–318. ISSN: 15459993.

[47] K. Yamasaki et al. "Roles of Tyr122-hydrophobic cluster and K+binding in Ca2+-releasing process of ADP-insensitive phosphoenzyme of sarcoplasmic reticulum Ca2+-ATPase". In: *Journal of Biological Chemistry* 283.43 (Oct. 2008), pp. 29144–29155. ISSN: 00219258.

[48] M. J. Moutin and Y. Dupont. "Interaction of potassium and magnesium with the high affinity calcium-binding sites of the sarcoplasmic reticulum calcium-ATPase". In: *Journal of Biological Chemistry* 266.9 (Mar. 1991), pp. 5580–5586. ISSN: 00219258.

[49] M. Musgaard, L. Thøgersen, and B. Schiøtt. "Protonation states of important acidic residues in the central Ca 2+ ion binding sites of the Ca 2+-ATPase: A molecular modeling study". In: *Biochemistry* 50.51 (Dec. 2011), pp. 11109–11120. ISSN: 00062960.

[50] K. R. Sipido and W. G. Wier. "Flux of Ca2+ across the sarcoplasmic reticulum of guinea pig cardiac cells during excitation contraction coupling." In: *The Journal of Physiology* 435.1 (Apr. 1991), pp. 605–630. ISSN: 14697793.

[51] C. H. Luo and Y. Rudy. "A dynamic model of the cardiac ventricular action potential: I. Simulations of ionic currents and concentration changes". In: *Circulation Research* 74.6 (June 1994), pp. 1071–1096. ISSN: 00097330.

[52] T. R. Shannon et al. "A mathematical treatment of integrated Ca dynamics within the ventricular myocyte". In: *Biophysical Journal* 87.5 (Nov. 2004), pp. 3351–3371. ISSN: 00063495.

[53] D. K. Ceholski et al. "Lethal, hereditary mutants of phospholamban elude phosphorylation by protein kinase A". In: *Journal of Biological Chemistry* (2012). eprint: `http://www.jbc.org/content/early/2012/06/15/jbc.M112.382713.full.pdf+html`.

[54] E. R. Higgins, M. B. Cannell, and J. Sneyd. "A buffering SERCA pump in models of calcium dynamics". In: *Biophysical Journal* 91.1 (2006), pp. 151–163. ISSN: 00063495.

[55] J. T. Koivumäki et al. "Modelling sarcoplasmic reticulum calcium ATPase and its regulation in cardiac myocytes". In: *Philosophical Transactions of the Royal Society A: Mathematical, Physical and Engineering Sciences* 367.1896 (June 2009), pp. 2181–2202. ISSN: 1364503X.

[56] Z. Zhang et al. "Detailed characterization of the cooperative mechanism of Ca2+ binding and catalytic activation in the Ca2+ transport (SERCA) ATPase". In: *Biochemistry* 39.30 (2000), pp. 8758–8767. ISSN: 00062960.

[57] J. Dhitavat et al. "Mutations in the sarcoplasmic/endoplasmic reticulum Ca2+ ATPase isoform cause Darier's disease". In: *Journal of Investigative Dermatology* 121.3 (Sept. 2003), pp. 486–489. ISSN: 0022202X.

[58] A. Hovnanian. "SERCA pumps and human diseases." In: *Sub-cellular biochemistry* 45 (2007), pp. 337–63. ISSN: 0306-0225.

[59] A. Xu, C. Hawkins, and N. Narayanan. "Phosphorylation and activation of the Ca(2+)-pumping ATPase of cardiac sarcoplasmic reticulum by Ca2+/calmodulin-dependent protein kinase." In: *Journal of Biological Chemistry* 268.12 (1993), pp. 8394–7. eprint: `http://www.jbc.org/content/268/12/8394.full.pdf+html`.

[60] P. A. Kollman et al. "Calculating Structures and Free Energies of Complex Molecules: Combining Molecular Mechanics and Continuum Models". In: *Accounts of Chemical Research* 33.12 (2000). PMID: 11123888, pp. 889–897. eprint: `https://doi.org/10.1021/ar000033j`.

[61] J. P. Glaves et al. "Phosphorylation and mutation of phospholamban alter physical interactions with the sarcoplasmic reticulum calcium pump". In: *Journal of Molecular Biology* 405.3 (Jan. 2011), pp. 707–723. ISSN: 00222836.

[62] C. G. Schipke et al. "Temperature and nitric oxide control spontaneous calcium transients in astrocytes". In: *Cell Calcium* 43.3 (Mar. 2008), pp. 285–295. ISSN: 01434160.

[63] B. J. Chun et al. "Simulation of P2X-mediated calcium signalling in microglia". In: *The Journal of Physiology* (). eprint: `https://physoc.onlinelibrary.wiley.com/doi/pdf/10.1113/JP277377`.

[64] L. M. Espinoza-Fonseca and D. D. Thomas. "Atomic-level characterization of the activation mechanism of serca by calcium". In: *PLoS ONE* 6.10 (Oct. 2011). Ed. by C. M. Stultz, e26936. ISSN: 19326203.

[65] E. F. Pettersen et al. "UCSF Chimera A visualization system for exploratory research and analysis". In: *Journal of Computational Chemistry* 25.13 (), pp. 1605–1612. eprint: `https://onlinelibrary.wiley.com/doi/pdf/10.1002/jcc.20084`.

[66] E. L. Wu et al. "CHARMM-GUI Membrane Builder toward realistic biological membrane simulations". In: *Journal of Computational Chemistry* 35.27 (2014), pp. 1997–2004. ISSN: 1096-987X.

[67] S. Jo et al. "CHARMM-GUI: A web-based graphical user interface for CHARMM". In: *Journal of Computational Chemistry* 29.11 (2008), pp. 1859–1865. ISSN: 1096-987X.

[68] W. L. Jorgensen et al. "Comparison of simple potential functions for simulating liquid water". In: *The Journal of Chemical Physics* 79.2 (1983), pp. 926–935.

[69] A. D. MacKerell et al. "All-Atom Empirical Potential for Molecular Modeling and Dynamics Studies of Proteins". In: *The Journal of Physical Chemistry B* 102.18 (1998), pp. 3586–3616.

[70] A. D. MacKerell, M. Feig, and C. L. Brooks. "Improved Treatment of the Protein Backbone in Empirical Force Fields". In: *Journal of the American Chemical Society* 126.3 (2004), pp. 698–699.

[71] J. C. Phillips et al. "Scalable molecular dynamics with NAMD". In: *Journal of Computational Chemistry* 26.16 (2005), pp. 1781–1802. ISSN: 1096-987X.

[72] J.-P. Ryckaert, G. Ciccotti, and H. J. Berendsen. "Numerical integration of the cartesian equations of motion of a system with constraints: molecular dynamics of n-alkanes". In: *Journal of Computational Physics* 23.3 (1977), pp. 327–341. ISSN: 0021-9991.

[73] T. D. Romo, N. Leioatts, and A. Grossfield. "Lightweight Object Oriented Structure analysis: Tools for building Tools to Analyze Molecular Dynamics Simulations". In: *Journal of Computational Chemistry* 35.32 (2014), pp. 2305–2318.

[74] D. R. Roe and T. E. Cheatham. "PTRAJ and CPPTRAJ: Software for Processing and Analysis of Molecular Dynamics Trajectory Data". In: *Journal of Chemical Theory and Computation* 9.7 (2013), pp. 3084–3095.

[75] J. S. Høye and L. Blum. "The mean spherical model for asymmetric electrolytes: Thermodynamics and the pair correlation function". In: *Molecular Physics* 35.1 (Jan. 1978), pp. 299–300. ISSN: 13623028.

[76] J. N. Herrera and L. Blum. "Sticky electrolyte mixtures in the Percus Yevick/mean spherical approximation". In: *The Journal of Chemical Physics* 94.7 (Apr. 1991), pp. 5077–5082. ISSN: 0021-9606.

[77] P. Li et al. "Rational Design of Particle Mesh Ewald Compatible Lennard-Jones Parameters for +2 Metal Cations in Explicit Solvent". In: *Journal of Chemical Theory and Computation* 9.6 (2013), pp. 2733–2748.

[78] C. N. Nguyen, M. K. Gilson, and T. Kurtzman Young. "Structure and Thermodynamics of Molecular Hydration via Grid Inhomogeneous Solvation Theory". In: *arXiv.org* arXiv:1108.4876 (2011).

[79] C. N. Nguyen, T. Kurtzman Young, and M. K. Gilson. "Grid inhomogeneous solvation theory: Hydration structure and thermodynamics of the miniature receptor cucurbit[7]uril". In: *The Journal of Chemical Physics* 137.4 (2012), p. 044101. eprint: `https://doi.org/10.1063/1.4733951`.

[80] K. Haider et al. "Solvation Structure and Thermodynamic Mapping (SSTMap): An Open-Source, Flexible Package for the Analysis of Water in Molecular Dynamics Trajectories". In: *Journal of Chemical Theory and Computation* 14.1 (2018). PMID: 29161510, pp. 418–425. eprint: `https://doi.org/10.1021/acs.jctc.7b00592`.

[81] N. Smith and E. Crampin. "Development of models of active ion transport for whole-cell modelling: cardiac sodium  potassium pump as a case study". In: *Progress in Biophysics and Molecular Biology* 85.2 (2004). Modelling Cellular and Tissue Function, pp. 387–405. ISSN: 0079-6107.